Design, Fabrication, and Characterization of a Floating-Gate Double Quantum Well Far-Infrared Photoconductor

Elżbieta Ledwosinska

Department of Electrical & Computer Engineering
McGill University
Montréal, Canada

September 2009

Under the supervision of Professor Thomas Szkopek.

A thesis submitted to McGill University in partial fulfillment of the requirements for the degree of Master of Electrical Engineering.

2009/09/01

Abstract

The design, fabrication, and characterization of a GaAs/AlGaAs double quantum well long-infrared photoconductor are reported. The double quantum well structure was designed using a 1-D Schrödinger-Poisson solver to fine-tune the material composition, thickness, and doping to control the 2-D electron gas (2DEG) subband energies, positions, carrier densities, and lifetimes of transitions. The wafer was grown commercially and devices were fabricated using cleanroom facilities at McGill and the Université de Montréal. The device has a floating gate architecture with perpendicular carrier transport, in contrast with the parallel transport scheme employed by almost all commercial detectors, where the photocurrent is measured directly. Perpendicular transport provides greater photoconductive gain than parallel transport, as seen in the high responsivities achieved by competing groups. The device reported herein was engineered to increase the coupling, and thus the responsivity, between the two wells by ≈ 40 % over the best previously reported results. The fabricated devices were tested under various temperature, biasing, and illumination conditions and fundamental properties of the device such as responsivity, sensitivity, and stability were characterized. The peak photoresponse has been observed for modulation frequencies from 20 Hz to 1 kHz, and is clearly discernible up to 30 K. The device exhibits a responsivity of $80 - 160$ A/W. This result is in fair competition with QWIPs demonstrating responsivities of mA/W -10 A/W. The device shows a NEP $= 4.7 \times 10^{-11}$ W/$\sqrt{\text{Hz}}$, and D$^* = 1.7 \times 10^8$ cm$\sqrt{\text{Hz}}$/W.

Abrégé

La planification, fabrication et charactérization d'un double puit quantique photoconducteur en longue-infrarouge de GaAs/AlGaAs sont présentés. La structure du double puit quantique a été créée avec le programme 1-D Schrödinger-Poisson solver afin de bien ajuster la composition des matériaux, les épaisseurs et le dopage afin de controler les énergies des sous-bandes, les positions, les densits de transporteurs des charge et les dures de vies de transitions du gaz d'électrons bi-dimensionel (2DEG). La plaquette a été fabriquée commercialement et les dispositifs ont été fabriqués dans les salles blanches de l'Université McGill et l'Université de Montréal. Le dispositif a une architecture à la grille flottante avec transport de charge perpendiculaire contrairement au concept de transport parallèle utilisé par presque tous les détecteurs commerciaux où le photocourant est mesuré directement. Le transport perpendiculaire donne un gain photoconductif plus grand que dans la géométrie parallèle comme démontré par les plus grandes responsivités produites par les compétiteurs. Le dispositif a été créé afin d'augmenter le couplage et améliore donc la responsivité entre les deux puits de ≈ 40 % de plus que les meilleurs résultats publiés. Les dispositifs fabriqués ont été testés à différentes températures, différents voltages et différentes illuminations. Les propriétées fondametales du dispositif comme la responsivité, la sensibilité et la stabilité ont été mesurées. La photoréponse maximale a été observée sous des fréquences modulatrices entre 20 Hz et 1 kHz et est clairement visible jusqu'à 30 K. Le dispositif démontre une responsivité de $80 - 160$ A/W. Ce résultat est à la hauteur avec QWIPs qui démontre des responsivité allant de mA/W -10 A/W. Ce dispositif démontre NEP $= 4.7 \times 10^{-11}$ W/$\sqrt{\text{Hz}}$ et D* $= 1.7 \times 10^{8}$ cm$\sqrt{\text{Hz}}$/W.

Acknowledgments

First and foremost, I would like to thank my supervisor, Dr. Thomas Szkopek, for providing endless insight, ideas, and encouragement. From my beginning as a neophyte in fabrication and the field of detector design, Prof. Szkopek's advice and explanations proved invaluable to my progress. At times when the light detectors had me in the dark, Prof. Szkopek was always ready with motivating suggestions that conjured new energy to proceed.

Also, I extend gratitude to the cleanroom staff at the Université de Montréal for training, answering extra questions, and accommodating my specific equipment requests. Also, gratitude is expressed for Dr. Richard Martel and Dr. Pierre Levesque for assisting me with the use of their low-temperature probe station.

I would like to thank Peter Gaskell for his technical expertise, such as rendering my break-out box elegant and showing me Vectorworks. Thanks to Helgi Skuli Skulason for saving me time with his Labview tips, and Vicknesh Shanmugan for helpful cleanroom conversations. Special thanks to the other members of our lab: Jonathan Guillemette for French assistance, and Shadi Sabri, Shahriar Al Imam, and Chris Rodenchuk, for various discussions along the way.

Last but not least, I would like to acknowledge my family for unfaltering support, and my boyfriend, for sharing my excitement with his stimulating questions, and helping me introduce patience to my approach.

Contents

List of Figures

List of Tables

Chapter 1

Introduction

Terahertz (THz) waves, which lie between infrared and microwaves in the electromagnetic spectrum, have recently been the subject of intense scientific investigation. Detectors and sources in this wavelength range of $0.3 - 30$ THz are comparatively new and undergoing much research to improve responsivity, detectivity and integration into imaging arrays. In Fig. 1.1 [1], we see the electromagnetic spectrum with the location of THz waves. The development of emitters and detectors in each spectral range has allowed the accumulation of knowledge in various sectors. Currently the search is ongoing for successful THz detectors, which will surely give rise to new industries.

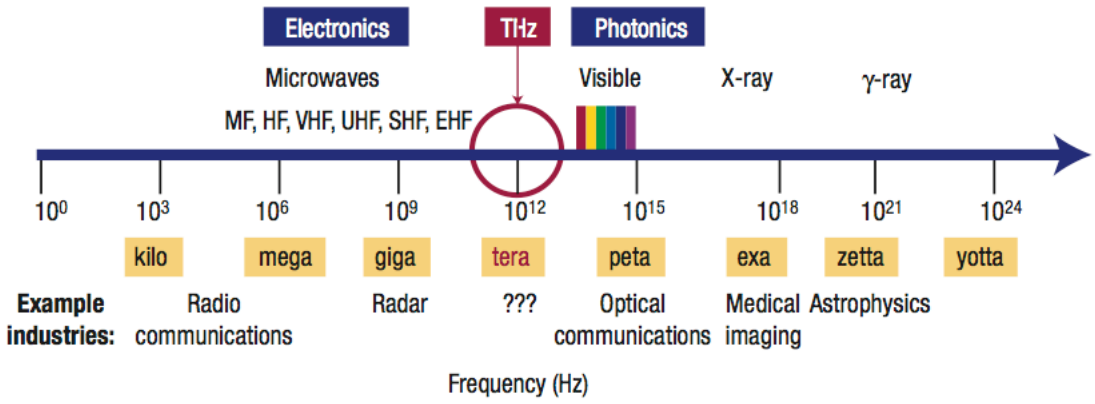

Fig. 1.1 The electromagnetic spectrum. The development of efficient THz detectors will give rise to new industries.

1.1 Motivation

THz radiation is fully harmless and can be used to discern organic compounds, metal objects, and sub-mm features. Designing and fabricating THz detectors is pertinent to a vast array of applications, from observing narcotics and explosives in a security setting, to mapping out the earliest evolutionary stages of galaxies, stars, and planets. Also, since THz radiation is readily absorbed by water, further applications include biomedical imaging to detect and diagnose cancers in the body, since cancerous tissue typically has a higher water content than healthy tissue [2].

We will explore various examples to illustrate the pertinence of advancing THz detectors.

1.1.1 Characterization of materials

Material reflection, refraction, absorption or emission of THz radiation provides information unseen in other frequency bands. For example, THz spectroscopy can be used to measure the carrier concentration and mobility of doped semiconductors such as GaAs and Si [3]. Imaging of dry dielectric substances such as paper, plastics, and ceramics can also be achieved [4]. These materials are relatively non-absorbing in the $0.2 - 5$ THz range, but one can distinguish between different materials by their refractive index, extracted from THz phase information. The advantage of THz imaging here over X-rays is that these materials are opaque at optical frequencies and X-ray images suffer from low contrast [1]. While non-polar, non-metallic solids such as plastics and ceramics are at least partially transparent and reflective in the $0.2 - 5$ THz range, any polar material, e.g. water, is highly absorptive, since dipole rotation frequencies are in the THz band, leading to strong resonant absorption.

As an example, Zhong *et al.* from Lockheed Martin Space Systems reported the detection of space shuttle foam insulation defects using a 0.2 THz Gunn diode oscillator (illumination source), a pyroelectric camera, and a Golay cell and Si Schottky diode as detectors. The space shuttle sprayed-on foam insulation (SOFI) has a low refractive index and absorption coefficient in the THz frequency range, which allowed non-destructive identification of the size and location of any defects [5].

1.1.2 Security

A great concern in our world today is the sensing of weapons and explosives; public awareness of requirements for security screening at airports has recently intensified. We are familiar with the X-ray for metal objects and swabbing for explosives, “al-

though in effect this capability may be more a matter of deterrence than detection" [6]. THz radiation would lend itself to such applications for three major reasons [7]:

1. THz radiation is readily transmitted through most non-metallic and non-polar mediums, including clothes, to be able to "see" the potential hazards.

2. Many explosives such as C-4, HMX, RDX, and TNT and chemical and biological agents possess characteristic THz spectra for simple identification. Many illegal drugs such as methamphetamines are also identifiable through THz spectra.

3. Due to the low-energy nature of the radiation, THz radiation poses no or minimal health risk to the suspect and/or operator.

While millimetre wave imaging (MMW) operating at a discrete frequency of ≈ 30 GHz is also suitable for sensing and security applications, THz detection does hold certain advantages, such as a spatial resolution that is ten times better than MMW, since the THz wavelength is roughly ten times shorter than MMW radiation. Also, as discussed earlier, THz detection offers specificity, i.e. the THz spectroscopic signatures of some explosives and other chemicals can be used as fingerprints to identify potential threats. There are no analagous spectroscopic spectra in the MMW range.

1.1.3 Illegal substance detection

THz waves are also suitable for drug detection, with many illicit drugs exhibiting fingerprint spectra in the THz region. Kawase et al. [8] demonstrated a THz spectroscopic imaging system by extracting the spatial distribution of drugs inside an envelope using absorption spectra and a Q-switched Nd:YAG laser, a TPO (THz

parametric wave oscillator), and a pyroelectric detector. Drugs could be sensed at concentrations of 20 mg/cm^2, and the authors reported to have isolated and extracted spatial patterns of each component even in situations involving a mixture or layers of various drugs. Thus, THz detectors have a large potential application for screening packages, security, and quality diagnosis.

1.1.4 Biomedical characterization

The collective vibrational modes of many proteins and DNA molecules lie in the THz range; thus THz spectroscopy can cast light on the conformational state of biomolecules. For example, THz spectroscopy can differentiate between single and double-stranded DNA from changes in refractive index [9]. In addition, Nagel et al. showed in 2002 [10] that a THz sensing system can detect DNA mutations of a single-base pair with femtomole sensitivity.

1.1.5 Array detectors

In the realm of marketable detectors, array detectors allow one to simultaneously register the photoresponse at multiple spatial points, as would a camera to form an image. In a focal plane array, each pixel is composed of a photoconductor, photodiode, or bolometer. Commonly used read-out circuitry is charged-coupling device (CCD) technology, or complementary metal-oxide semiconductor (CMOS) technology. A few examples of these array detectors include [11]:

1. Microbolometer arrays for thermal imaging cameras, where incident photons cause an increase in the temperature of the elements, which causes a change in resistance that is then read out by the external circuit. Vanadium oxide (VOx)

microbolometer arrays offer hundreds of thousands of pixels, each ≈ 25 μm in size and sensitive to the mid-infrared.

2. Photoconductive arrays, also used in the mid-infrared region, operate when a photon with energy greater than the bandgap of a material such as InSb or HgCdTe, creates an electron-hole pair, which results in a detectable current.

3. Quantum well infrared photodetectors (QWIPS) used in megapixel focal-plane arrays can provide long-wavelength infrared (LWIR) and mid-wavelength infrared (MWIR) images by using GaAs/AlGaAs and GaAs/InGaAs/AlGaAs elements, respectively.

There also exist arrays fabricated from p-i-n photodiodes, such as InGaAs and HgCdTe used in the visible and infrared. Schottky barrier photodiode elements are used in FPA cameras, as in PtSi, which is easily manufactured and highly stable, despite having low quantum efficiency in the infrared.

1.2 Thesis contributions

THz technology is on the forefront of research in a field that possesses the solutions to many important and urgent issues in our world today. We have fabricated and tested a GaAs/AlGaAs double quantum well heterostructure based on a floating gate architecture first developed by Komiyama [12] for ultra-sensitive THz detection. We have designed and simulated the double-quantum well structure using a 1-D Schrödinger-Poisson solver program, which allowed us to engineer the 2DEG subbands, densities, and lifetimes of transitions. The wafer was commercially grown by molecular beam epitaxy (MBE) at IQE Inc. (Bethlehem, PA), and the detectors were fabricated using

state-of-the-art fabrication facilities at the Université de Montréal and McGill. The material composition and doping was designed to provide two quantum wells, each populated by a 2-dimensional electron gas (2DEG). When a THz photon ionizes the electrons in the first well via an intersubband transition, the conductivity of the second well is modulated. This floating gate architecture uses perpendicular transport, in contrast with the parallel transport scheme employed by almost all commercial detectors, where the photocurrent is measured directly. Perpendicular transport provides greater photoconductive gain than parallel transport because the lifetime for charge separation is longer, and the mobility of the carriers in the detection current is higher [13]. The fabricated devices were tested under various temperatures and illumination conditions, and fundamental properties of the device such as responsivity, sensitivity, and stability were characterized. Contributions of our device to the field of developing marketable THz detectors include:

1. Highest demonstrated electrical bandwidth of a floating gate photoconductor.

2. A responsivity better than conventional QWIPs.

The flow of information pertaining to the field of THz photodetectors and the presentation of our device will proceed as follows:

Chapter 2:

An overview of THz photodetection will be outlined. The figures of merit, such as responsivity, for these devices will be defined and we will discuss a brief history of various photoconductors developed to date.

Chapter 3:

We will describe the theory and design of the heterostructure, from the 1-D Schrödinger-

Poisson simulations employed to fine-tune the device parameters for THz detection, to the simulation of transmission characteristics of the device.

Chapter 4:

Here we will delve into the details of the initial testing of the grown wafer and the clean-room fabrication of the device itself.

Chapter 5:

Finally, we will discuss the measurement set-up, and the characterization of the device as a THz photoconductor under various illumination and biasing conditions.

Chapter 2

THz photodetector overview

2.1 Figures of Merit

We review here the figures of merit that are commonly used to evaluate the performance of photoconductors. Many of these figures of merit apply to photodetectors more general than photoconductors [14].

2.1.1 Quantum efficiency

Quantum efficiency, η, is the probability that a single incident photon generates a mobile photoelectron and/or photohole through a process such as interband absorption, intersubband absorption or photoionization (also referred to as bound-to-free state absorption). A low quantum efficiency may arise due to reflection from the surface of the detector, weak interaction (low absorption cross-section) between electrons and incident photons, or immediate recombination of electron-hole pairs near

the semiconductor surface. The quantum efficiency can be written as:

$$\eta = \zeta \left(1 - R\right) \left(1 - e^{-\alpha d}\right), \tag{2.1}$$

where R is the power reflectance at the surface, ζ is the fraction of electron-hole pairs that contribute to the detector current, α the absorption coefficient of the material (per cm), and d is the depth of the photoconductor active region. Since α and R are dependent on wavelength, so is the quantum efficiency.

2.1.2 Responsivity

The responsivity of a photodetector is the ratio of the measurable electrical signal to the input optical signal power,

$$\mathcal{R} = \frac{I}{P}. \tag{2.2}$$

If every photon resulted in one photoelectron that contributes to the measured photoconductor current, a photon flux ϕ would yield a current i of:

$$i = e \cdot \phi. \tag{2.3}$$

So, an optical power of

$$P = h \cdot \nu \cdot \phi \tag{2.4}$$

would yield a current

$$i = \frac{e \cdot P}{h \cdot \nu}. \tag{2.5}$$

Taking into consideration that only a fraction, η, of photons actually contributes to the response the electric current is:

$$i = \eta \cdot e \cdot \phi = \frac{\eta \cdot e \cdot P}{h \cdot \nu}, \tag{2.6}$$

which gives a quantum limit for responsivity:

$$\mathcal{R} = \frac{\eta e}{h\nu} \tag{2.7}$$

in the absence of any photoconductive gain. The quantum limit for responsivity applies to photodiodes in the absence of avalanche multiplication.

2.1.3 Response time

The time constant of the detector electrical response, τ, can be expressed as:

$$\tau = RC = \rho\epsilon, \tag{2.8}$$

where R and C are the resistance and capacitance associated with the device, respectively, and ρ and ϵ are the resistivity and permittivity of the semiconductor material. Fundamentally, τ is limited by the traversal time for an electron through the device.

2.1.4 Gain

The recombination time and transit time for mobile electrons in a photoconductor can differ. For example, if a photon liberates an electron from a donor atom, an excess mobile electron will contribute to conduction until an electron is trapped by

the donor. Put succinctly, a single photon absorption can cause multiple traversals of the device by an electron. The expected number of transits across the active region is the photoconductive gain, G:

$$G = \frac{\tau}{\tau_e}, \tag{2.9}$$

where τ is the excess-carrier recombination lifetime, or in other words the lifetime of charge separation, and

$$\tau_e = \frac{L}{v_e} \tag{2.10}$$

is the electron transit time across the sample (length of the sample L divided by velocity of the carrier v_e). For a device exhibiting gain G, the charge q delivered to the circuit by a single electron-hole pair would be:

$$G \cdot e = q. \tag{2.11}$$

However, the opposite may also take place. If the recombination lifetime is sufficiently short such that carriers recombine before ever reaching the edge of the sample, $\tau < \tau_e$ and the gain is less than one. This may occur if there is a sufficient population of carriers of the opposite type for recombination. Thus, one sees that the ratio of the traversal time to the drift time of a single carrier determines whether the gain is high or low. When a gain is present, the responsivity may now be expressed as:

$$\mathcal{R} = G\frac{\eta \cdot e}{h \cdot \nu}. \tag{2.12}$$

From the above equations, we see that responsivity can be increased at the expense of the charge separation lifetime.

2.1.5 Noise Equivalent Power

Noise equivalent power (NEP) is the signal power required to obtain unity signal to noise ratio in the presence of detector or background noise [11]. The minimum radiant-flux level discernable by a detector is dependent on the detector noise. The signal to noise ratio (SNR) can be expressed in terms of responsivity as:

$$\frac{S}{N} = \frac{(\mathcal{R}\phi)^2}{i_n^2}, \tag{2.13}$$

where $\mathcal{R}$ is the responsivity, ϕ is the radiant flux (W), and i_n is the noise current. The noise equivalent power is the optical power that leads to a unity SNR, thus,

$$\text{NEP} = \frac{i_n}{\mathcal{R}}. \tag{2.14}$$

Again, since the responsivity is a function of wavelength and frequency, so is the NEP. To compare the NEP of one detector to another, one must also take into account the optically active area, the noise-equivalent electrical bandwidth, the spectral operating region, the optimum bias, and the operating temperature. Thus, the NEP is situationally specific, which renders it difficult to use as a performance factor.

A better figure of merit is the normalized detectivity, D*:

$$\text{D}^* = \frac{\sqrt{A\Delta f}}{\text{NEP}} = \frac{\mathcal{R}\sqrt{A\Delta f}}{i_n}. \tag{2.15}$$

Here, the sensitivity of the device is normalized to a 1 cm^2 area A and 1 Hz noise equivalent bandwidth, which allows easy comparison. Another interpretation for D* is the SNR from a 1 cm^2 detector with 1 W of incident power and a bandwidth of

1 Hz. The units of D* are cm$\sqrt{\text{Hz}}$/watt, as defined by Jones [15].

2.1.6 Background Limited Infrared Photometry (BLIP)

If the background photon flux is larger than any detector noise, the precision of radiation measurements is governed by BLIP. For example, infrared and submillimeter telescopes are limited by the 3 K submillimeter background radiation [16]. The detector temperature must be less than the background temperature in order to observe the background, as a consequence of Kirchoff's Law. D* and NEP are dependent on temperature, and cooling is required to achieve BLIP conditions [11]. For a cooled photoconductor, the detectivity under BLIP conditions is expressed as:

$$\mathrm{D}^*_{blip} = \frac{\lambda}{2hc}\sqrt{\frac{\eta}{E_{background}}}, \tag{2.16}$$

where $E_{background}$ is the background photon irradiance. The detector operating temperature required to achieve BLIP conditions is an important figure of merit, due to the expense and weight of cooling equipment.

2.2 Overview of photodetectors

2.2.1 Photodiodes

One of the simplest types of photodetectors is the p-n photodiode. This device consists of a p-n junction whose reverse current increases as it absorbs photons with absorption coefficient α. Since a p-n junction can transport carriers due to the electric field in the depletion layer, the electron-hole pairs generated by the photons contribute to the current. The response time of these devices is hindered by carriers generated outside

the depletion layer, which take some time to diffuse into it, a relatively slow process in comparison with drift. These devices can be enhanced by inserting an intrinsic layer of material between the p and n layers, to form a p-i-n photodiode. The advantage here is a widening of the depletion layer. This in turn allows a greater available area for capturing light, a reduced junction capacitance and thus RC time constant, and a reduced ratio between the diffusion length and the drift length of the device, ensuring a larger fraction of the generated current is carried by the faster drift process.

Heterostructure photodiodes are formed from two semiconductors of different bandgaps. The advantage of such a design is that a large-bandgap material ($E_g > h\nu$) can minimize optical absorption outside the depletion region, which yields the name "window layer". Common heterostructure designs have included $Al_xGa_{1-x}As/GaAs$ in the wavelength range $0.7-0.87$ μm, and $In_xGa_{1-x}As/InP$, which can be tuned over $1300-1600$ nm, of interest in optical fibre communications. $Hg_xCd_{1-x}Te/CdTe$ is useful because HgTe and CdTe can be lattice-matched at most compositions, with a compositionally tunable bandgap between 3 and 17 μm. These devices are used for night vision, thermal imaging, and long-wavelength lightwave communications. Then, there exist quaternaries, such as $In_{1-x}Ga_xAs_{1-y}P_y/InP$ and $Ga_{1-x}Al_xAs_ySb_{1-y}/GaSb$, used in the $0.92-1.7$ μm range. The fourth element provides an additional degree of freedom to allow lattice matching for different values of E_g.

Schottky-barrier photodiodes are metal-semiconductor heterojunctions. Instead of the p or n layer in the p-n junction diode, a thin, semi-transparent metal film is used. Schottky-barrier structures are majority-carrier devices with inherently fast responses and large operation bandwidths. One can acquire such devices with response times of picoseconds, with bandwidths of $\approx$ 100 GHz [17]. Excess noise sources beyond

thermal or shot noise, such as $1/f$ or flicker noise, must be regarded when judging the usefulness of any diode detectors. The responsivity of typical diodes (Virginia Diodes, Inc.) ranges from 4000 V/W at 100 GHz to 400 V/W at 900 GHz [18]. The detectors show $\tau \ll 1$ ns, with broad operational bandwidth and high sensitivity, exhibiting excellent NEP of $\approx$1.5 pW/$\sqrt{\text{Hz}}$ near 150 GHz, and $\approx$20 pW/$\sqrt{\text{Hz}}$ at 800 GHz. The Schottky diode detector can operate at ambient or cryogenic temperatures and has a fast response time compared to other room temperature sensors such as Golay cells, pyroelectric detectors, or bolometers [18]. In 1992, Peatman *et al.* [19] proposed a high-frequency diode for use as a frequency multiplier element in the mm and sub-mm wavelength regions. Typically, Schottky barrier diodes are used as frequency multiplier elements for local oscillator (LO) sources.

Due to the low photon energies associated with THz frequencies ($1 - 10$ meV), the ambient background thermal noise and intrinsic detector noise almost always dominate narrow-band signals. Thus, THz detectors require cryogenic cooling, long-integration times, or both. The crossover frequency at which an ideal thermal noise limited detector (e.g. a room-temperature Schottky barrier diode), surpasses the sensitivity of an ideal quantum detector (e.g. a photodiode), occurs between $1 - 10$ THz. Space-qualified heterodyne receivers have been fabricated for operation up to 2.5 THz, which may possibly be extended to higher frequencies, but is limited by the availability of local oscillators with power levels approaching 1 mW [17].

2.2.2 Golay cell

The Golay cell [20] is a photo-acoustic device, with ambient operating temperature and broad spectral response. It is composed of a 6 mm HDPE (high density polyethylene)

input window and a small gas chamber including a thin partially absorbing film called the "optical microphone section". Impinging THz or infrared radiation is absorbed by the thin film inside the gas cell, heating the gas, which expands and distorts the mirrored back wall of the cell. Using an LED, optics, grating, and photodiode, the distortion is monitored, with the output of the photodiode proportional to the displacement of the mirrored wall.

2.2.3 Bolometers

Bolometers operate by sensing a change in the resistance of a material as a result of a change in temperature due to impinging radiation. Bolometers stretch back to the 1940s, with the invention of the first liquid He cooled superconducting device for the far IR [21]. The NEP of the superconducting device was almost 2×10^{-11} W/$\sqrt{\text{Hz}}$, exceeding that of all other detectors at the time. A helium-cooled carbon bolometer, developed by Boyle and Rogers in 1959 [22], offered an NEP of 5×10^{-12} W/$\sqrt{\text{Hz}}$ and in 1961, Low [23] developed an He-cooled Ge bolometer with an NEP of 5×10^{-13} W/$\sqrt{\text{Hz}}$. In 1963 an InSb bolometer was created by Kinch and Rollins [24], with an electron gas used as the heat-sensing medium, and a sensitivity equal to Low's device. However, the response time was about three orders of magnitude smaller than for the Ge bolometer. In 1969, Drew and Sievers [25] developed a Ge bolometer cooled to 0.37 K with an NEP of 3×10^{-14} W/$\sqrt{\text{Hz}}$ for use in the far IR.

Bolometers are popular in sub-mm astronomy instruments, such as the second Sub-millimetere Common User Bolometer Array (SCUBA-2), a "CCD" style sub-mm camera on the James Clerk Maxwell Telescope in Hawaii. The bolometers are TES (transition edge sensor) detectors, which seize advantage of the large variation of

resistance with temperature through the superconducting transition [26]. However, this instrument uses a dilution fridge to cool the detector stage to 160 mK. The predecessor to SCUBA-2, SCUBA-1, was forced to permanently retire from service early after suffering a ^{4}He gas leak for several months prior. This example again illustrates the pressing need for far-infrared detectors suitable for integration into a focal plane array that do not require extreme cooling for operation.

2.2.4 Pyroelectric detector

The basic principle of pyroelectric detectors composed of materials such $LiTaO_3$ is as follows:

Below the Curie temperature, these materials show large spontaneous electrical polarization, which changes if the temperature is altered due to incident radiation. If electrodes are placed at opposite faces of a slice of the material, effectively forming a capacitor, the change in polarization will produce a voltage across the capacitor, which can be read out if the external impedance is relatively high. Because the temperature may change for all wavelengths of incident radiation, filters are used to manufacture pyroelectric sensors for different wavelengths [27].

2.2.5 Field Effect Transistors

In 1993, Dyakonov and Shur [28] demonstrated that electrons in a ballistic field effect transistor can provide a new mechanism for the generation of tunable far-infrared electromagnetic radiation. In 1998, Lu and Shur [29] reported the first implementation of a THz detector utilizing the 2-D electron gas in a high electron mobility transistor (Fujitsu FHR20X HEMT) operating at 2.5 THz with a responsivity of 600 V/W.

In 2006, Fatimy *et al.*[30] used high electron mobility GaN/AlGaN transistors as detectors in the $0.2 - 2.5$ THz frequency range. The experiments were performed at temperatures ranging from $4 - 300$ K, with a resonant response understood as plasma wave oscillations in the gated 2DEG. The authors claimed that these devices could operate at high temperatures and in harsh environments due to the nitride material properties. The best NEP was reported to be 5×10^{-9} W/$\sqrt{\text{Hz}}$, which, while still slightly higher than commercial detectors such as Golay cells, pyroelectric detectors, and Schottky diodes, provides the advantage of operation at high sampling frequencies in the THz range.

2.2.6 Quantum Well Infrared Photo-transistors

The advent of quantum well infrared photodetectors (QWIPs) lies with Esaki and Chang in 1974 [31], who investigated electronic transport properties in GaAs/AlAs periodic structures, or "superlattices" prepared by molecular beam epitaxy (MBE). Superlattices were first investigated by Esaki and Tsu in 1970 [32], before the invention of MBE.

The first QWIP was demonstrated by Levine *et al.* in 1987 [33]. This structure was based on 50 periods of GaAs wells and AlGaAs barriers between n+ GaAs contact layers. The thickness and composition, as for our design, were chosen to provide exactly two bound states in the well separated by an energy level in the THz range (here, $\lambda = 10 \ \ \mu$m). The photoexcited electrons tunnel out of the first well when the electron executes the intersubband transition from the bound ground state to the bound excited state after absorbing an infrared photon. The photocurrent is produced by the electrons which have escaped their wells and are propelled forward for a distance

L (mean free path for recapture back into a well) in the medium above the wells by the application of an electric field for an excited lifetime τ_L. These electrons produce the photocurrent. The situation where the photocarrier is transported along the quantum well direction with an applied parallel bias voltage is known as parallel transport; our device operates on the principle of perpendicular transport. If the voltage is applied perpendicular to the growth direction, the current is measured inside the well itself, known as perpendicular transport. In the latter scenario, the difference between the excited-state and ground-state mobilities is much larger, which yields a larger photoresponse [34]. Also, because the heterobarriers block the transport of carriers in the doped quantum-well ground state, the dark current is lower.

The drift velocity above the barriers of parallel transport QWIPs is typically $v_s = 5 \times 10^6$ cm/s, and the hot-carrier recapture lifetime is $\tau_L = 40$ ps. Thus, these QWIPs are ideal for ultrahigh-frequency heterodyne detection due to their high speed in combination with their narrow spectral response.

Other materials besides GaAs and AlGaAs can be used to fabricate QWIPs, such as $In_{0.53}Ga_{0.47}As/In_{0.52}Al_{0.48}As/InP$ lattice-matched heterostructure. With a conduction band discontinuity of $\delta_{Ec} = 550$ meV, significantly higher than $GaAs/Al_xGa_{1-x}As$, shorter wavelength operation can be achieved for direct-gap QWIPs of $\lambda \approx 4$ μm. Another example is $In_{0.53}Ga_{0.47}As/InP$, $\lambda \approx 8$ μm, which has been studied for optical communication sources and detectors, witih a maximum responsivity of 2 A/W at 20 K and bias voltage $= -4$ V. InGaAs/InP ($\lambda = 8 - 12$ μm) typically show responsivities of 6 A/W. p-QWIPs can also be produced, but demonstrate detectivity an entire order of magnitude worse than n-QWIPs as a result of their large effective mass and short hot-hole lifetime, i.e. short mean free path L.

Multiwavelength QWIPs can be produced, as with all designs, by controlling the quantum well width, barrier composition, and structure. With these structures, the peak response can be varied from $2 - 20+$ μm. Devices such as that of Faska *et al.* [35] operate at $\lambda = 4.6$ and 10 μm. Another example is a QWIP operating in the midwave ($\lambda = 3 - 5$ μm) and long-wave ($\lambda = 8 - 10$ μm) regions, demonstrated by Kheng *et al.* [36]. This structure is composed of a wide well with two bound states, and doped very heavily ($N_d = 6.8 \times 10^{18}$ /cm^3) such that the Fermi level lies above the second state. The key to this voltage-tunable detector lies in the high doping, which allows one to observe both the E_1 and E_2 bound-to-bound intersubband absorption (at $\lambda \approx 10$ μm) and bound-to-continuum absorption ($\lambda \approx 4$ μm).

In comparison with the popular HgCdTe photodetectors, QWIPs lack performance at higher temperatures due to their low quantum efficiencies, especially above 70 K. While QWIPs exhibit quantum efficiencies around 10 %, HgCdTe detectors show $70 - 90$ % with an anti-reflection coating. Also, wide-band spectral sensitivity allows use of a smaller aperture and a greater collection efficiency, which renders HgCdTe focal plane arrays useful for imaging and spectral radiometry. However, several properties of QWIPs, such as high impedance, fast response time, and lower power consumption, are also suitable for FPA fabrication. There appears to be better pixel uniformity using QWIPs, and the established industrial infrastructure in III-V material device and growth for GaAs devices in telecommunications offers QWIPs an optimism not available to HgCdTe, which are to date only used for IR detectors. Currently, QWIP and HgCdTe FPAs are limited by the parameters of the read-out circuit, and so reveal similar figures of merit [37].

In Table 2.1, we compare a few popular detectors on the market (Golay cells, pyro-

electric sensors, and HgCdTe photodiodes) with current QWIPs under development.

2.2.7 Quantum-Dot Infrared Photodetector (QDIP)

QDIPs resemble QWIPs, but the quantum wells are replaced by quantum dots. In a QDIP, as in conventional QWIP operation, electrons are excited from their bound states inside the dots into the continuum above, causing an observable photocurrent [42]. One of the advantages of QDIPs over QWIPs is the capability of normal incidence absorption, i.e. that light normal to the wafer growth direction can cause intraband absorption, which is not the case for QWIPs, which require a coupling mechanism to ensure components of the optical electric field are suitable for absorption [34]. Another advantage is lower dark current due to reduced electron-phonon scattering. These advantages are largely due to the 3-dimensional confinement of the quantum dot. The most popular QDIPs are composed of self-assembled InAs dots on GaAs substrates.

The single photon QDIP, developed by Komiyama in 2000 [43], uses a cold (50 mK) single electron transistor (SET), and quantum dot in a high magnetic field. Photon absorption occurs when the photon energy is equal to the energy difference between the Landau levels in the 2DEG, which results in a shift of the gate voltage of the SET due to electron tunneling. The detector sensitivity is 0.1 photons/s per 0.1 mm^2 detector area. The device is suitable for signals in the range of $1.4 - 1.7$ THz. The NEP $= 10^{-22}$ W/$\sqrt{\text{Hz}}$, which is more than 1000 times more sensitive than the best bolometric devices. One drawback is the speed of the detector: ≈ 1 ms.

2.2.8 Quantum Dot in a Well (DWELL)

One can reap the advantages of QDIPs while maintaining reproducible recipes for the operating wavelength, as for QWIPs, by integrating quantum dots directly with QWIPs to form a DWELL, such as the work of S. Krishna [44]. Here, the author presented devices consisting of InAs quantum dots embedded in InGaAs quantum wells that exhibited multi-spectral response. Recent work by Andrews *et al.* [45], compares a DWELL FPA to a commercially available QWIP FPA. Though the DWELL array demonstrated a better SNR, the responsivity for the QWIP was an order of magnitude larger than for the DWELL. This new technology anticipates improved performance as further work is conducted.

2.2.9 Floating gate photoconductor

Our device is based on the work of An *et al.* [12]: an infrared (14.5 μm) phototransistor on a GaAs/AlGaAs double quantum well heterostructure. When a THz photon ionizes the electrons in the first well, an intersubband energy transition occurs, which we can measure by a change in the conductivity of the second well. This technique is known as perpendicular transport. The other almost exclusively used technique for commercial detectors is parallel transport, where a photon excites an electron to tunnel out of the well and produce a photocurrent that is directly measured in the continuum above the wells. Perpendicular transport provides greater sensitivity than parallel transport because the charge separation lifetime is greater and the mobility of carriers in the detection current is higher, both factors contributing to a high photoconductive gain. The parallel transport structure suffers from relatively low electron mobilities and short charge separation lifetimes ($1 - 10$ ps). The basic principle is a photosensitive

floating gate, whose operation is depicted in Fig. 2.1. The upper well, through application of gate voltages, serves as an isolated conducting island. When IR photons are absorbed in the top well with enough energy to overcome the first well barrier, the alloy ramp provides an electric field to guide the electrons quickly down to the bottom well, where they are absorbed. Through capacitive coupling, the conductance of the bottom well is increased. An *et al.* achieved a responsivity of 10^3 A/W (10^4 A/W with a reset operation to avoid saturation [46]), the highest in this wavelength range.

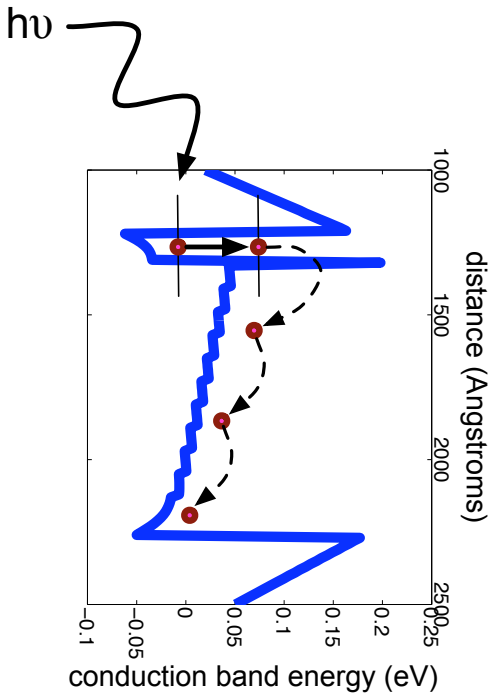

Fig. 2.1 The operating principle of a floating gate photoconductor. Application of negative gate voltages forms an electrically isolated 2DEG in the upper quantum well, which serves as a floating gate that is capacitively coupled to the 2DEG in the lower well. Upon impingement of a THz photon in the upper well, excited electrons tunnel into the bottom well, changing the conductance in the lower source-drain channel.

Table 2.1 Comparison of IR photodetectors on the market with QWIPs.

Detector	R (A/W)	D^* (cm$\sqrt{\text{Hz}}$/W)	Range (THz)	Advantages	Disadvantages
Golay cell ([38], [39])	10^4	7×10^9	$0.02 - 20$	Large sensing area. Sensitive to $<$ nA.	Slow response time: 25 ms. Physically large.
Pyroelectric ($LiTaO_3$) ([38], [39])	10^3	4×10^8	$0.02 - 3$	Inherently fast: μs$-$ms. Operating temp.: -5 $-$ 120°C.	THz response not well established. Microphonic response.
HgCdTe photodiodes ([40])	10^5	10^{14}	$21 - 38$	Easy band-gap tailoring. $\eta \geq 70$ %	Non-uniformity over large area. High cost of growth/processing.
QWIPs ([34], [41], [12])	$10^{-3}-$ 10^3	$2 \times 10^{10}-$ 2×10^{13}	$20 - 60$	Uniformity over large area. Established, low-cost GaAs growth technologies.	$\eta \leq 10$ % Require low operating temperature.

Chapter 3

Theory and Design of Heterostructure

The double quantum well structure was designed using a 1-D Schrödinger-Poisson solver. The material composition, thickness, and doping were all fine-tuned to control the 2DEG subband energies, positions, carrier densities, and lifetimes of transitions. These parameters were engineered to provide two quantum wells, such that an electron in the top well subject to THz radiation would tunnel into the bottom well, causing a measurable increase in the conductance of the bottom well. Simulations taking into account non-ideal behaviour, such as less than fully-ionized carriers, were also performed to ensure the design would yield a fully operational detector. Also, the electron transmission characteristics of the device were modeled at various temperatures.

3.1 Design of the material composition of the wafer

Our device design is based on the pioneering work of Komiyama's group in Japan, and aimed to increase the capacitive coupling between the upper and lower wells by decreasing the separation of the electron states in the upper and lower wells. While An *et al.* demonstrated a device with a separation of 151 nm between the first and second electron subbands, our design yields a simulated separation between upper well and lower well electron states of 94 nm, which is a 38 % decrease. This is expected to:

1. Increase the induced charge polarization in the lower well in response to the photoionization of the upper well.

2. Decrease the likelihood of photoelectron capture by interface traps and un-ionized donors.

The final design with all optimized parameters consists of: a semi-insulating GaAs substrate, buffer layers of GaAs and AlGaAs/GaAs superlattices, 100 nm GaAs, a 90 nm spacer layer of $Al_{0.3}Ga_{0.7}As$, Si-δ-doping ($6.2\times10^{11}/cm^2$), a 30 nm $Al_{0.3}Ga_{0.7}As$ spacer layer, a 14 nm GaAs quantum well, 75 nm of composition-graded $Al_xGa_{1-x}As$ ($x = 0.00 - 0.10$) barrier layers, a 1 nm $Al_{0.3}Ga_{0.7}As$ tunnel barrier, a 10 nm GaAs quantum well, a 25 nm $Al_{0.3}Ga_{0.7}As$ barrier layer, Si-δ-doping ($1.06 \times 10^{12}/cm^2$), an 85 nm $Al_{0.3}Ga_{0.7}As$ barrier, and a 10 nm GaAs cap. The Si-δ-doping supplies electrons to the two quantum wells.

In Table. 3.1, we list the layers for growth.

Table 3.1 Layers of the heterostructure wafer. N_d refers to n-type doping concentration.

	surface	
100 Å	GaAs	
850 Å	$Al_{0.3}Ga_{0.7}As$	
Si-δ-doping	$Al_{0.3}Ga_{0.7}As$	$N_d = 1.06 \times 10^{12}$ /cm^2
250 Å	$Al_{0.3}Ga_{0.7}As$	
100 Å	GaAs	
10 Å	$Al_{0.3}Ga_{0.7}As$	
750 Å	AlGaAs - composition graded $Al_{0.1}Ga_{0.9}As$ $\Downarrow$ $Al_{0.01}Ga_{0.99}As$	
140 Å	GaAs	
300 Å	$Al_{0.3}Ga_{0.7}As$	
Si-δ-doping	$Al_{0.3}Ga_{0.7}As$	$N_d = 6.20 \times 10^{11}$ /cm^2
900 Å	$Al_{0.3}Ga_{0.7}As$	
1000 Å	GaAs	
	AlGaAs/GaAs superlattices	
	GaAs buffer	
	semi-insulating GaAs substrate	

3.2 Schrödinger-Poisson simulations

The heterostructure conduction energy bands were simulated using Prof. Gregory Snider's 1-D Poisson-Schrödinger solver from the University of Notre Dame, IN. In Fig. 3.1, we see the conduction band energy at 10 K for the entire structure with the main layers labeled.

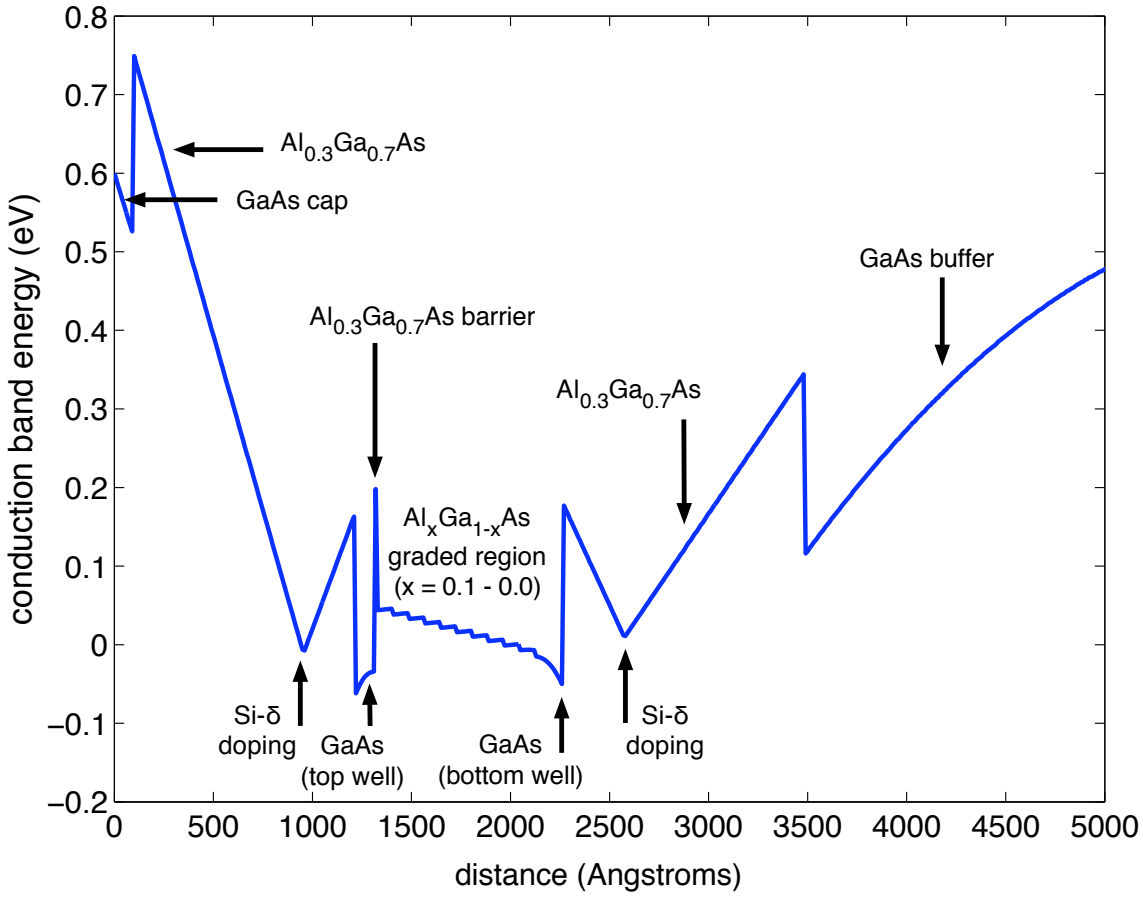

Fig. 3.1 Conduction band energy at 10 K and main structure of the device.

The electron densities in the two wells, the separation of electron subbands, and

the expected transmission function of the electrons out of the first well and into the second well upon receipt of a THz photon were all calculated and tuned by changing parameters of the device structure. Controllable parameters comprised thickness and material composition of the various layers, as well as doping concentration. These parameters were optimized to provide the structure yielding only one occupied electron subband per well at 10 K, with electron densities approximately divided equally between the top and bottom wells, and with the shortest possible spatial separation between the two electron subbands. Also, high electron densities in the top and bottom wells were desired. The final requirement of the structure was a transmission function that permitted resonant THz photon-assisted tunneling of electrons from the top well to the bottom well. Simulations were also carried out for situations where only $40 - 60$ % of the donors were ionized, as the ionization fraction of donors is difficult to predict, and can vary in experimental situations according to the rate of device cool down and exposure to visible or IR light. In addition, an expected pinch-off voltage (voltage at which the top well carrier density drops to approximately 0.1 % of its original value) was calculated to be -0.843 V at 4.2 K.

In order to plot the conduction and valence energy bands, we adopt a Hartree-Fock approximation to the electron-electron interaction in the quantum wells. The 1-D Schrödinger-Poisson method iterates between three equations to provide a self-consistent solution for the electrical properties of a 1-D structure. The three equations are:

1. The Schrödinger equation to calculate the electron wavefunctions:

$$\left[\frac{-\hbar^2}{2m^*}\frac{d^2}{dz^2} + E_c(z)\right]\psi_j(z) = \epsilon_j\psi_j(z), \tag{3.1}$$

where $E_c(z)$ is the conduction band edge potential, and ϵ_j is the energy of the continuous wavefunction $\psi_j(z)$, and m^* is the effective mass of the electron in GaAs: 0.067 of the free electron mass.

2. The Fermi-Dirac distribution to find the electron carrier density $n(z)$:

$$n(z) = g\sum_j |\psi_j(z)|^2 f(E_j, E_F) = 2\sum_j |\psi_j(z)|^2 \left(\frac{m^* k_B T}{\pi\hbar^2}\right) ln\left[1 + exp\left(\frac{E_F - \epsilon_j}{k_B T}\right)\right] \tag{3.2}$$

Here, g is the degeneracy factor (equal to 2 for spin) and $f(E_j, E_F)$ is the electron Fermi-Dirac distribution.

3. The Poisson equation to calculate the potential profile:

$$-\frac{d}{dz}\left[\epsilon(z)\frac{d}{dz}V(z)\right] = e^2\left[n(z) - p(z) + N_D(z) - N_A(z)\right], \tag{3.3}$$

where $n(z)$ and $p(z)$ and $N_D(z)$ and $N_A(z)$ are the electron and hole distributions and doping densities, respectively.

The 2-DEG carrier densities in the top and bottom wells were calculated according to [47]:

$$n_{2d} = \sum n_j \tag{3.4}$$

$$n_j = 2\frac{m^*}{\pi\hbar^2}\int_{\epsilon_j}^{\infty} f(E, E_F)dE = 2\frac{m^* k_B T}{\pi\hbar^2} ln\left[1 + exp\left(\frac{E_F - \epsilon_j}{k_B T}\right)\right] \tag{3.5}$$

Here, $f(E, E_F)$ is the Fermi-Dirac distribution function. n_j is the sheet density associated with each electron subband, and thus n_{2d}, the carrier density in each well, can be found by summing the n_j residing in each well. ϵ_j is the energy of each electron subband, and so $E_F - \epsilon_j$ is the Fermi level with respect to the sub-band energy.

Table 3.2 lists the characteristic parameters obtained for the final design.

In Fig. 3.2, we plot the conduction band energy of the final design. The two wells separated by the graded barrier are clearly evident, and we see the two electron subbands at 4.2 K.

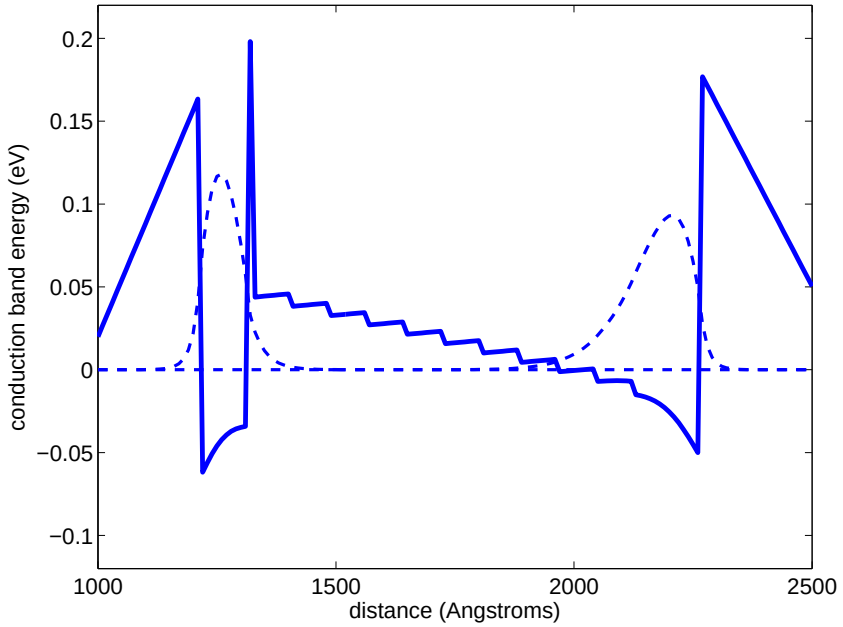

Fig. 3.2 Conduction band energies and electron wave functions at 4.2 K, as simulated for the photoconductor structure.

In Fig. 3.3, one sees the same structure simulated at 10 K, where three subbands exist in total, one in the first well and two in the second well. As the temperature is further increased, the number of subbands also increases, with 12 subbands at 300 K.

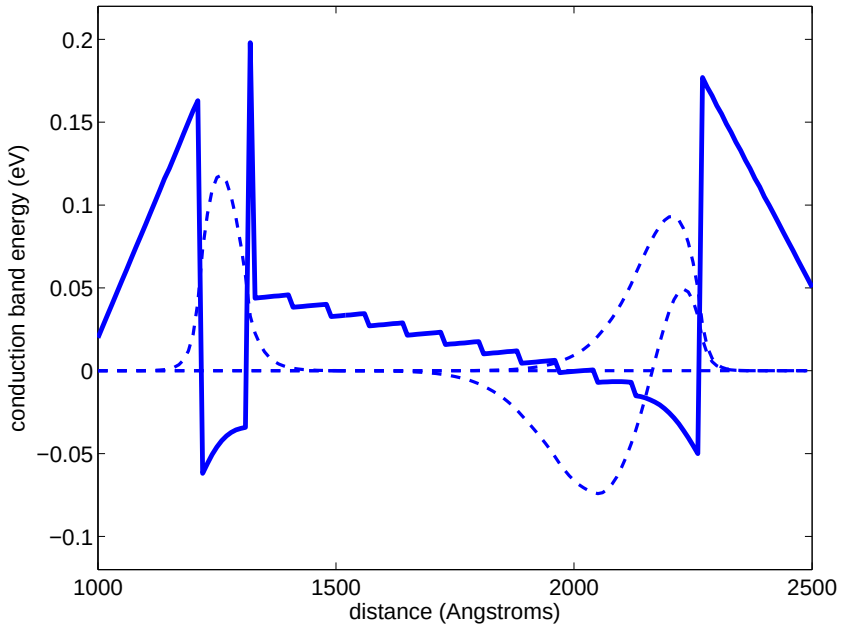

Fig. 3.3 Conduction band energies and electron wave functions at 10 K, as simulated for the photoconductor structure.

3.3 DX centres and donor ionization

Due to the theoretical nature of the modeling routine, there are a few unrealistic drawbacks to the 1-D Schrödinger-Poisson method, such as the assumption that all donors are fully ionized. These concerns demanded to be addressed in order to produce the optimal working detector.

The standard donor in AlGaAs is Si, which may exist in a second state known as the DX centre [47]. In this situation, the lattice relaxes around the donor upon embracing an electron, releasing extra energy so that the electron is more tightly bound. The energy of the DX centre varies with x in $Al_xGa_{1-x}As$; for pure GaAs, it lies within the conduction band, for $x > 0.2$ it lies below, and it may return to

the X-minima of the conduction band as x tends towards 1. Thus, the effect of DX centres is to trap carriers within an energy barrier, requiring excess energy beyond that expected for Si from a simple hydrogenic model. The binding energy $E_{dd} \approx 0.12$ eV for $x = 0.3$, and the radius of the wavefunction is reduced to atomic scale. In order to characterize the energies associated with the binding, one must consider: the barrier to occupation of the DX centre, a second barrier to release the electron from the donor, and E_{dd}, which governs the occupation if the DX centres are in thermal equilibrium with the rest of the crystal. Because the barriers for entry and exit are high, thermal equilibrium is difficult to achieve at low temperature, and it is experimentally found that the occupation of DX centres "freezes" below 150 K, resulting in metastable occupation of traps. Thus, the device may actually demonstrate fewer carriers during a cool-down than originally modeled, which will be detrimental to its performance as a photoconductor.

To ensure a design robust to the effect of DX-centres, less than fully-ionized carriers were simulated by inputting only $40-60$ % of the starting dopant density into the 1-D Schrödinger-Poisson program. It was verified that even with less than fully-ionized carriers, the remaining carrier densities would still provide a structure with sufficient 2DEG carrier densities to demonstrate optimal performance.

One method to remove electrons from their DX centres is via persistent photoconductivity. Using an infrared source with energy below the bandgap (an LED is ideal) can excite electrons out of their DX centres, increasing the donor ionization and hence increasing the density of mobile electrons. Due to the retrapping barrier, the electrons tend to remain free at low temperatures.

3.4 Transmission calculations

A fundamental concern in designing this photoconductor structure was fine-tuning the tunneling transport of the electrons over the first barrier and into the second well. This process was simulated in Matlab by calculating the electron transmission function of the first steep barrier and the successive graded barrier leading to the second well. Variations involving different material compositions, widths of barriers and wells, doping concentrations, and combinations thereof were all explored at 4.2, 10, 77, and 300 K, yielding a final design with parameters listed in Table 3.2. At 77 K, the energy difference between the first and second electron subbands in the first well is 0.0998 eV, which corresponds to a wavelength of 12.4 μm, or 24 THz. (The design of An *et al.* yields 90 meV = 14 μm = 21 THz.)

To simulate the transmission coefficient of an arbitrary sequence of steps and plateaus, we used a transmission matrix (T-matrix) formalism [47].

The T-matrix for a potential step from region 1 to region 2, T_{21}, where k_1 and k_2 are the wave vectors of the electrons in the medium before and after the potential step, is:

$$T_{21} = \frac{1}{2k_2} \begin{bmatrix} k_2 + k_1 & k_2 - k_1 \\ k_2 - k_1 & k_2 + k_1 \end{bmatrix} \tag{3.6}$$

If we express T_{21} with symbolic matrix elements, we have:

$$T_{21} = \begin{bmatrix} T^{11} & T^{12} \\ T^{21} & T^{22} \end{bmatrix} \tag{3.7}$$

The reflection and transmission flux coefficients, R and T, can be recovered from

the elements of T_{21} as follows:

$$R = \left| -\frac{T^{21}}{T^{22}} \right|^2 \tag{3.8}$$

$$T = \left| \frac{T^{11}T^{22} - T^{12}T^{21}}{T^{22}} \right|^2 . \tag{3.9}$$

For an electron traveling a distance d through a region with constant kinetic energy, the T-matrix T_d for such a translation is:

$$T_d = \begin{bmatrix} e^{ik_1 d} & 0 \\ 0 & e^{-ik_1 d} \end{bmatrix} \tag{3.10}$$

Transmission through an arbitrary potential profile can be approximated by successive multiplication of T-matrices for potential steps and translations. The goal of this design was to ensure the transmission coefficient was effectively zero for electrons in the top well at the Fermi energy until an impinging photon in the THz energy range provided enough energy for an electron to overcome the first transmission barrier and fall into the second well. Thereafter, the transmission coefficient should rise to 1.0.

The aim was to produce a lifetime on the order of ms in the first well, as this signifies that electrons will remain in the first well under ambient conditions and it will be the action of the THz photon that will provide the necessary energy for the intersubband transition (ISBT) for the electron to escape the well. The time an

electron spends in the first well, τ, is:

$$\tau = \frac{1}{f \cdot T}, \tag{3.11}$$

where T is the transmission coefficient for the electron to transfer into the second well.

The frequency of traversal, f, in the first well is calculated according to:

$$f = \frac{v_g}{2d}, \tag{3.12}$$

where d is the width of the first well, 10 nm.

The group velocity of the electron waves are expressed as:

$$v_g = \frac{\hbar k_{E_f}}{m^*}, \tag{3.13}$$

where k_{E_f} is the wave vector taken at the Fermi energy, and m^* is the effective mass of the electrons in GaAs, 0.067 of the electron mass.

As we can see in Fig. 3.4, the transmission function for our design is similar to that of the design of An *et al.*, while possessing a separation of 94 nm between the electron densities in the two wells, as opposed to An *et al.*'s separation of 151 nm. Also, one can see there is not much difference in the transmission characteristics of this design at 4.2 K and 77 K.

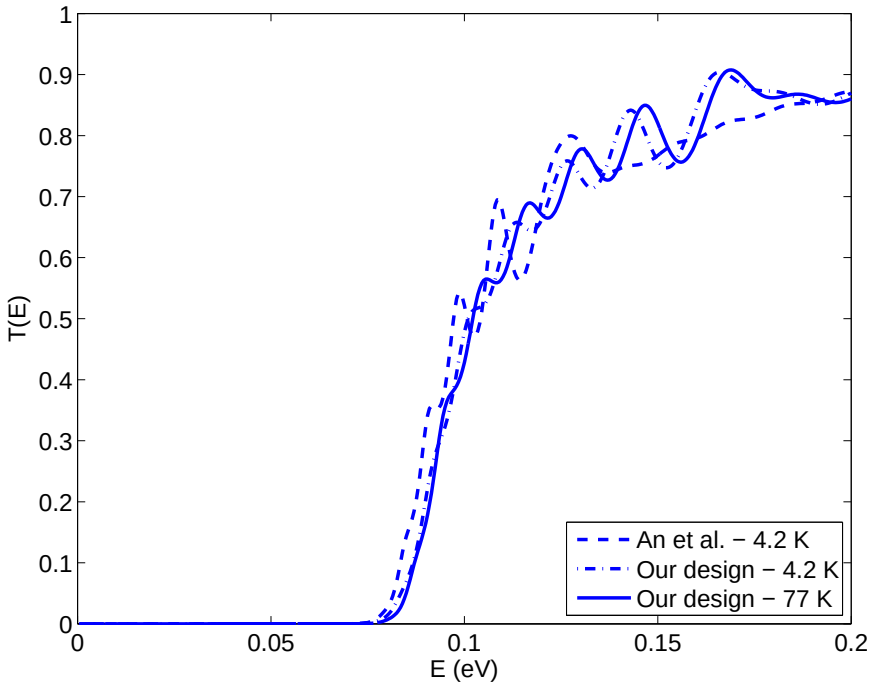

Fig. 3.4 Transmission flux coefficient: An *et al.* and our design at 4.2 and 77 K.

Table 3.2 Design Parameters

Temp. (K)	$n_{s,top}$ (/cm^2)	$n_{s,bot}$ (/cm^2)	N_{SB}	% (1, 2)	Sep. (nm)	E_f (eV)	T	τ (ms)	v_g (m/s)	f (THz)
4.2	4.19×10^{11}	3.40×10^{11}	2	51, 49	94	0.046	1.2×10^{-11}	3.3	4.9×10^5	24.5
10	4.19×10^{11}	3.40×10^{11}	3	48, 43	94	0.051	1.7×10^{-11}	2.3	5.2×10^5	25.8
77	4.05×10^{11}	3.12×10^{11}	9	51, 41	94	0.045	1.6×10^{-11}	254.6	4.9×10^5	24.3
300	2.92×10^{11}	2.13×10^{11}	12	38, 24	95	0.013	—	—	—	—

$n_{s,top}$	electron carrier density in the top well
$n_{s,bot}$	electron carrier density in the bottom well
N_{SB}	number of total electron subbands existent
% (1, 2)	percentages of the carriers residing in the first and second subbands
Sep.	separation between the carrier densities in the two wells
E_f	Fermi energy of the electrons in the top well
T	transmission coefficient for the electrons in the top well
τ	lifetime of the electrons in the top well
f	frequency of traversal of the electrons in the top well

Chapter 4

Device fabrication

Fabrication of devices on the commercially grown heterostructure wafer was performed in a Class 1000 cleanroom at the Université de Montréal. The fabrication steps included mesa formation, ohmic contacts, and Schottky gates, followed by packaging procedures in preparation for photoconductivity measurements in a 10 K cryostat.

4.1 Wafer growth and initial testing

The heterostructure design wafer, hereforth refered to as the wafer, was grown commercially at IQE Inc. (Bethlehem, Pennsylvania). Upon receipt of the wafer, we tested the sheet resistance using In contacts placed on the four corners of a 0.5×0.5 cm square sample. Thin slices of In wire were gently squeezed on the surface of the sample and annealed on a hot plate at 310°C for four minutes. The lowest resistance between the two best contacts was measured with a voltmeter to be ≈ 3 kΩ.

4.2 Cleanroom procedure

In preparation for fabrication, a photomask with the necessary layers for each photolithographic step was designed in Tanner L-Edit and sent to the UCLA Nanoelectronics Research Facility (NRF) to be patterned with a laser mask writer. We used modern GaAs/AlGaAs processing techniques, with the selection of contact metals and etchants aided by [48]. The basic outline for fabrication of the floating-gate phototransistor devices are enumerated as follows:

1. **Mesa formation:**

   Mesas were formed by a photolithography step followed by a wet etch using Piranha. The mesas were necessary to isolate the photoactive regions of each device on the die of 100 devices.

2. **Ohmic contacts**:

   Ohmic contacts were fabricated by photolithography, electron-beam metal deposition, and a rapid thermal anneal, so that one could apply a source-drain bias to induce and measure the current flowing through the device.

3. **Schottky gates**:

   Schottky gates were formed in a similar manner to the ohmic contacts and were necessary to apply a voltage to the top of the structure in order to modulate the electron densities in each well. Also, a grating pattern within the Schottky layer was fabricated on top of the photoactive region in order to couple the incoming radiation into the wells.

4. **Packaging**:

   The devices were cleaved, mounted, and wire-bonded to a Dual-Inline-Package

(DIP) chip carrier in preparation for measurements in a 10 K Closed Cycle Refrigerator System from Janis, (model CCS-150).

We will now discuss each step in detail.

4.2.1 Mesa formation

An ≈ 1 cm$\times 1$ cm square of the wafer was cleaved at McGill and taken to the Université de Montréal for fabrication. The sample was cleaned by soaking it in separate beakers of acetone, isopropyl alcohol (IPA), and de-ionized (DI) water consecutively for 5 minutes each, then blown dry with N_2 gas. It was dehydrated for 6 minutes on a hotplate at 150°C and let cool. AZ5214-EIR photoresist (PR) was spun at 500 rpm for 5 seconds, and 3000 rpm for 45 seconds. The sample was soft-baked at 105°C for 1 minute 20 seconds. A Karl Suss MA-4 mask aligner with a 274 nm Hg lamp was used to expose the mesa layer on the photomask for $12 - 12.5$ seconds for lamp intensities of $7 - 10$ mW/cm^2. Due to the large-scale features of this layer, precise optimization of the exposure time was superfluous. Then, the sample was developed for 45 seconds in a stirred mixture of AZ400K:DI-H_2O (1:4), followed by an $\approx$ 15 second rinse in DI water. The sample was then hard-baked at 120°C for 2 minutes. A measurement using a Dektak profilometer typically yielded a photoresist height of $\approx$ 1.8 μm.

The mesa etch was performed with a Piranha mixture composed of H_2SO_4:H_2O_2:H_2O (1:8:200 mL) for 1 minute 40 seconds. The measured etch rate was 2000 Å/min. The sample was then rinsed for ≈ 1 minute in DI-H_2O. The PR and mesa height together was about 2.2 μm. The sample was then stripped of resist by soaking it in separate beakers of acetone, IPA, and DI water consecutively for 5 minutes each, then blowing dry with N_2 gas. Residual photoresist was usually visually evident on the sample

at this point, so a descum procedure was necessary: 5 minutes, 200 mTorr, 100 W, oxygen plasma at 20 sccm. Now, we measured the mesa height, typically $\approx$ 3400 Å, enough to lie safely below the two wells.

4.2.2 Ohmic contacts

The ohmic photolithography was performed as follows: the sample was cleaned by spraying with acetone/IPA/DI-H_2O from the spray bottle, then blown dry and dehydrated for 6 minutes at 150°C. AZ5214-EIR photoresist was spun as in the mesa photolithography, and the sample was soft-baked for 1 minute 20 seconds at 105°C, and exposed as for the mesa. Then, there was a cross-link bake at 105°C for 1 minute, followed by a $140 - 140.5$ second (at $7 - 10$ mW/cm^2) flood exposure to effect image reversal. The sample was developed in the same manner as for the mesa, followed by a descum treatment of 100 W O_2 plasma at 200 mTorr, 20 sccm, for 1 minute. The descum treatment was necessary here to ensure there was no persisting resist that would inhibit contact of the metal that was to be deposited in the next step.

The ohmic contact pads were deposited via electron-beam deposition in a stack of Ni/Ge/Au/Ti/Au at thicknesses of 250/325/650/200/3000 Å, respectively. Liftoff was performed with acetone heated to 50°C. The sample was soaked for $\approx$ 10 minutes, gently agitated with spray from the acetone bottle, followed by a 5 minute rinse in IPA and DI-H_20. A descum procedure as after the photolithography step was performed.

The sample was then rapidly thermally annealed in a nitrogen atmosphere as follows:

1. Ramp from room temperature to 250°C in 30 seconds.
2. Hold at 250°C for 30 seconds.
3. Ramp to 410°C in 30 seconds.
4. Hold at 140°C for 60 seconds.
5. Cool to below 100°C and remove.

The flat, smooth ohmic contacts present before the rapid thermal anneal typically took on a bubbly, wrinkled appearance post-anneal. As expected, the contacts with fewer bubbles tended to be more resilient to peel-off during subsequent steps where any agitation, such as that due to cleaning, was involved.

Before proceeding to the next step, the contact resistance of the ohmic pads was tested on a probe station situated in the the cleanroom connected to a hand-held voltmeter. Devices fabricated on samples from the interior of the wafer exhibited contact resistances of ≈ 10 kΩ, while one trial of devices from the edge of the wafer yielded resistances of up to 20 kΩ, due to the defects and lower quality growth present at the edges of the wafer.

4.2.3 Schottky gates

Within the Schottky gate layer is a 7.5 μm period grating lying on top of the mesa, composed of an array of square metal pads where the ratio of open to metal-pad areas is unity. The purpose of the grating is to couple the incoming THz radiation into

the quantum well. That is, the intersubband transition requires that a component of the optical electric field lie perpendicular to the growth direction. An optimized 2D grating can enhance the responsivity of a device by a factor of $2-3$ relative to a bare aperture [34]. Samples with and without the grating Schottky layer were fabricated for testing. Without the grating the Schottky layer photolithography followed as for the ohmic procedure. Due to the 2.3 μm spacing between the grating squares in the Schottky layer with the grating, this step of photolithography demanded to be optimized to ensure the squares were developed acceptably, i.e. as close to the resolution of the original pattern on the mask as possible. Various tests with different spin speeds, bake times, exposure times, and developers, and edge-bead removal techniques finally yielded a recipe that provided satisfactory results. The sample was cleaned as usual and dehydrated for 5 minutes at 150°C. Photoresist AZ5214-EIR was spun at 500 rpm for 5 seconds and 5000 rpm for 35 seconds. This faster spin rate resulted in a thinner layer of photoresist (1.4 μm), which yielded better results since the edge-beads (photoresist at the edges) were not as high. Smaller edge beads ensured a firmer contact of the sample to the mask during the photolithography exposure, lessening diffraction effects. The sample was soft-baked at 105°C for 90 seconds and cooled for 5 minutes. It was then exposed for 16 seconds at a lamp intensity of $8.3-8.5$ mW/cm^2. A bake at 105°C for 1 minute followed, then the sample was flood-exposed for 160 seconds at the same lamp intensity. Finally, the sample was developed for a total of 75 seconds in AZ400K:DI-H_2O (1:4) and blown dry with N_2 gas.

Before the Schottky gate metal deposition, the sample was dipped in a Buffered Oxide Etchant (BOE): NH_4F:HF (7:1), for 15 seconds, followed by a rinse in DI

water for 10 seconds. To minimize native oxide growth, the sample was rushed to the electron-beam-deposition chamber and placed under vacuum as quickly as humanly possible. Within 15 minutes from exiting the BOE solution, the sample was mounted, loaded into the chamber, and the chamber evacuated to under $\approx 2 \times 10^{-6}$ Torr. The Schottky gate deposition consisted of: Ti/Pt/Au = 200/100/400 Å. Liftoff was performed as for the ohmic procedure, though sometimes the aid of an ultrasonic bath was required.

An optical micrograph of a finished device is given in Fig. 4.1.

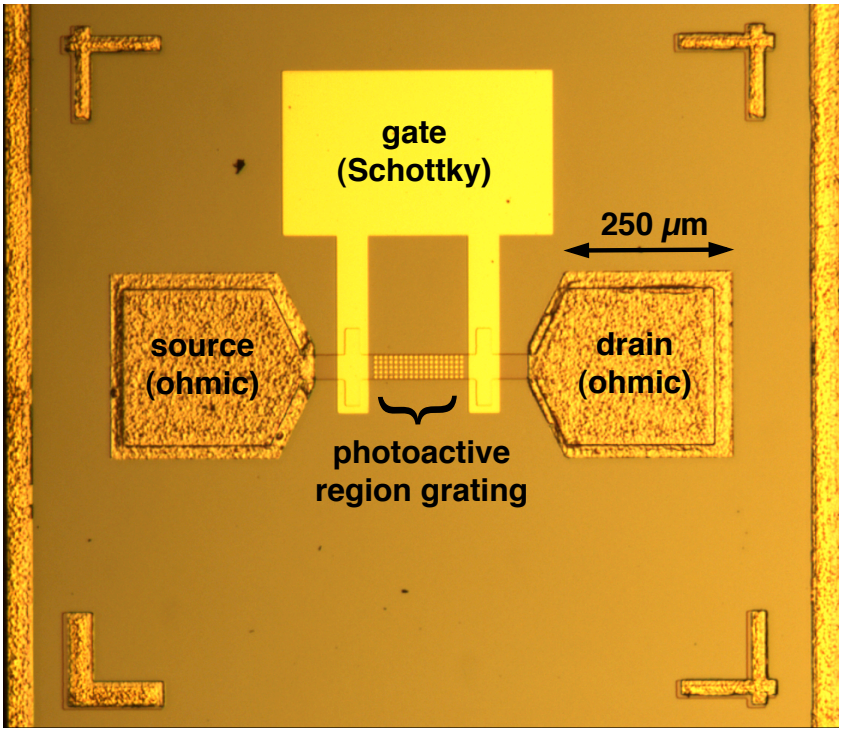

Fig. 4.1 The final fabricated device, with a Schottky gate, two ohmic contacts, and a grating to couple the incident radiation into the quantum wells.

4.2.4 Initial tests and packaging

A 1 cm×1 cm square of the Wafer would ideally yield 100 fabricated devices. However, the best yield achieved was $60-80$ %. Yield-limitation was caused by all unavoidable cleaning, agitation, and handling. Also, although the pre-metal-deposition descum procedure was optimized to ensure good contact of the ohmic stack to the devices, the rapid thermal anneal would still sometimes cause ohmic pads to peel off.

The sample was then placed in a 77 K probe station under $\approx 1 \times 10^{-7}$ Torr at the Université de Montréal, courtesty of Prof. Richard Martel. Using a Keithley 4200 measurement system, the I-V characteristic curve of each device was tested for a source-drain bias of 50 mV. Devices exhibiting gate currents on the order of μA were noted as leaky, and devices showing a high source-drain current (greater than 65 μA) were also recorded.

The square of fabricated samples was then cleaved into pieces small enough to fit on a 16-pin dual-inline-package (DIP) chip carrier. Silver epoxy was used to mount the small sample, and the contact pads were wire-bonded using Al wire at room temperature with a force of 20 g. Though silver epoxy is conductive, in our situation any low-temperature adhesive would have sufficed, as the substrate was semi-insulating. The sample was now ready for insertion into the 10 K closed-cycle optical cryostat for photoconductivity measurements.

Chapter 5

Photoconductor characterization

The devices were tested in a cryogen-free closed-cycle 10 K cryostat to reduce the temperature dependent noise current and to confine the electrons into the two separate quantum wells. The device behaviour was documented under various illumination, biasing, and temperature conditions.

For all light-response measurements, a KRS5 window (transmission window $0.6 - 40$ μm) was installed on the cryostat, and the light response explored through various filters: a 0.5 mm thick Si wafer (transmission window $1 - 10$ μm), a $7 - 14$ μm filter, or a $12 - 20$ μm filter. Light from a SiC globar at ≈ 1000 K was chopped using an optical chopper at various frequencies and a lock-in amplifier was employed to measure the photoresponse under different gate and source-drain voltages, chopping frequencies, and photoconductor temperatures.

5.1 Cryostat wiring

The 10 K cryostat (model CCS-150 from Janis) was wired to perform a voltage-biased current measurement with low noise. A sample chuck was machined to attach to the cryostat sample holder, and a chip-carrier socket was mounted onto a piece of breadboard that would permanently attach to to the sample holder. For each of the 16 pins on the chip-carrier socket, we used twisted-pair phosphor-bronze (PhBr) wire with one signal wire soldered to the pin and one ground wire leading to a common cold-ground connected to the cold head of the cryostat; refer to Fig. 5.1. The 34 gauge phosphor-bronze wire was chosen for its low electrical resistivity (11 μW·cm at 293 K) and low thermal conductivity (4.6 W/m·K at 10 K). Each signal and ground wire individually then passed through a 220 pF mica feed-through capacitor, where the signal wire was then connected to a BNC output on a breakout box, and the ground wire soldered to the BNC shell. With this arrangement, any sample in a DIP could quickly and easily be mounted onto the socket.

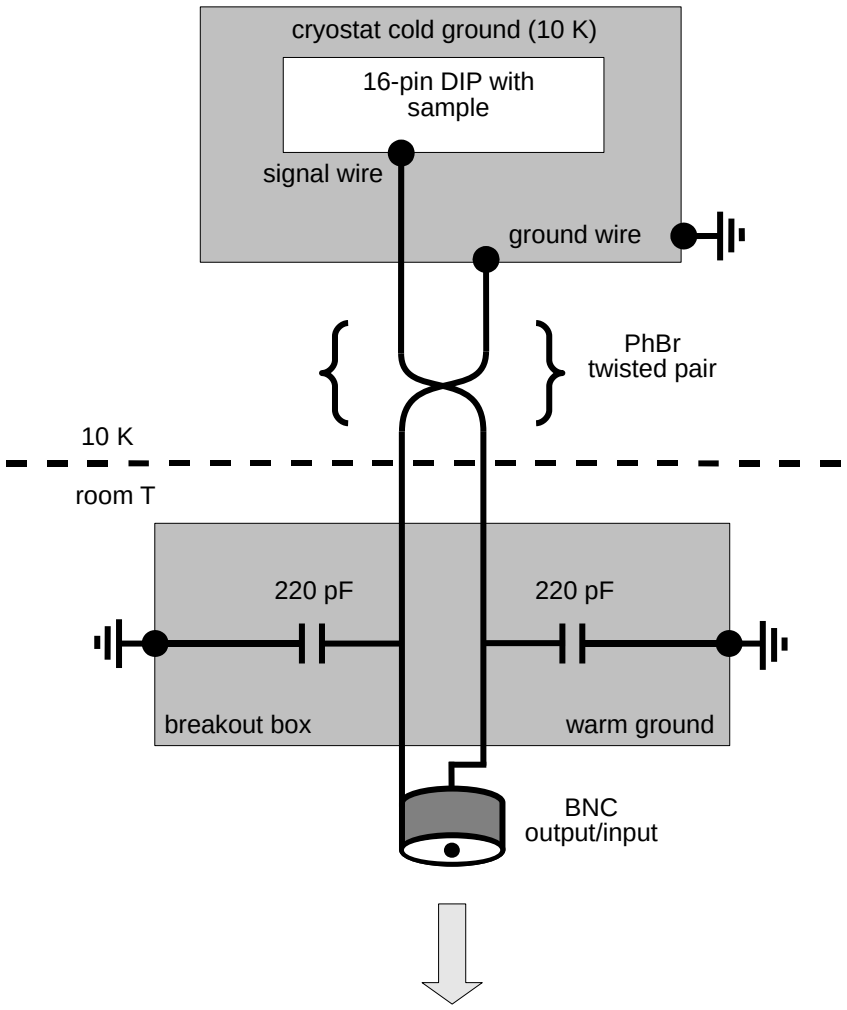

Fig. 5.1 Wiring schematic. Ground is indicated with grey.

The sample was biased with electronically controlled external battery sources (Stanford Research Systems SIM 928 isolated voltage sources), and the current from the drain was fed into a variable-gain low-noise current amplifier (Femto DLPCA-200) before the signal entered the lock-in amplifier. The 3 dB-bandwidth of the current

amplifier was 400 kHz and the input noise was 460 fA/$\sqrt{\text{Hz}}$ at the low-noise setting with transresistive gain 10^5 V/A. A Labview program was written to remotely control the lock-in amplifier (Stanford Research Systems SR830) and biasing electronics through a GPIB interface and to automate data collection. In Fig. 5.2, we see the measurement setup.

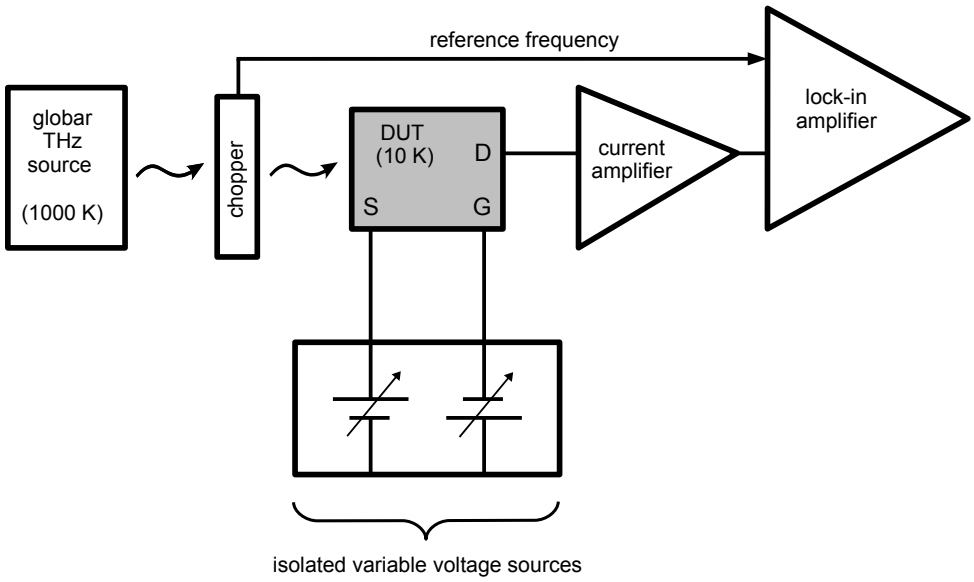

Fig. 5.2 Detector measurement setup. Grey indicates 10 K. All other objects, unless otherwise indicated, are at room temperature.

5.2 Basic characteristics of the device

The basic operation of the device can be explained as follows (refer to Fig. 5.3). As the gate voltage is swept negative, the top well 2DEG becomes electrically isolated

between the gates, with a charge of Q+ΔQ. When THz photons impinge on the top well, an intersubband transition occurs, whence the excited electrons (ΔQ) tunnel through the thin barrier and are rapidly guided to the lower quantum well along the electrostatic potential slope. The electrons are absorbed by the 2DEG in the lower quantum well, causing the upper quantum well to become positively charged. This positive charge in the isolated upper quantum well increases the electron density of the 2DEG in the bottom well via capacitive coupling. We then measure the increase in conductance, ΔI, through the lower channel.

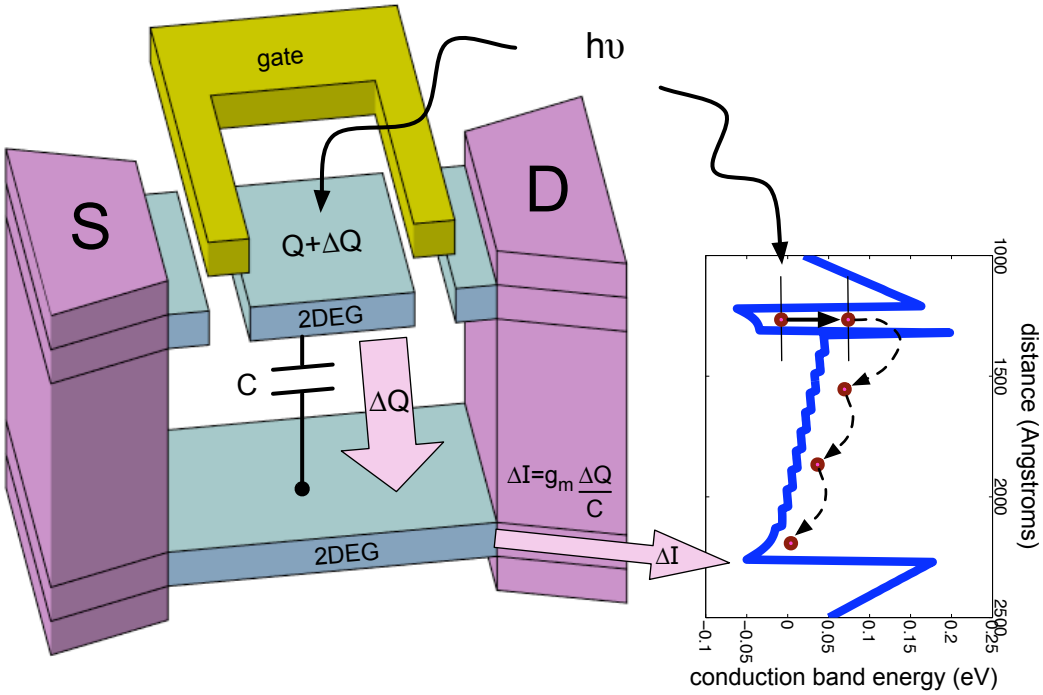

Fig. 5.3 Cross-sectional view of the device (left) and schematic representation of the detector mechanism (right). When a THz photon impinges on the electrically isolated 2DEG in the top well, an intersubband transistion occurs that causes electrons to tunnel through the thin barrier to the lower 2DEG channel. Due to capacitive coupling between the two wells, an increase in conductance is measured through the lower channel.

A typical I-V curve for the device exposed to the globar through the KRS5 window can be seen in Fig. 5.4, where the source-drain bias is fixed at 50 mV and the gate voltage is swept from 0 to −1.5 V. The current is highest at zero gate voltage, when all the electrons are in the top well and contributing to the conductance. The current decreases from that point onwards as the top well is depleted underneath the gates and forms a constricted island. Around −0.2 V, one can see a slight increase before the current begins to drop again. It is believed this slight increase may be due to the

cessation of electrons hopping from one energy to a higher energy band as the higher energy band becomes unavailable, and thus scattering is reduced. The current then continues to decrease until the gate voltage is low enough; at ≈ -1.2 V both the top and bottom wells are depleted and there is zero conduction.

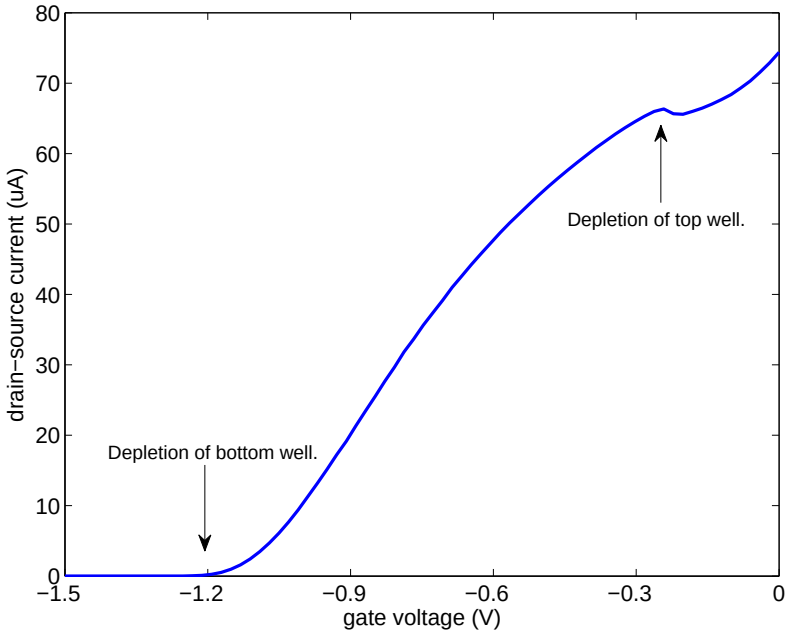

Fig. 5.4 I-V curve, $V_{DS} = 50$ mV, exposure to globar through KRS5. The device exhibits two quantum wells.

A certain interesting phenomenon was observed through the appearance and disappearance of a third well. As seen in Fig. 5.5, the third well appears at a much lower voltage than the designed second well, and the peak current at the pinchoff of the second well and the beginning of conduction through the third well is far lower than the current at the pinchoff of the first well and the beginning of conduction through the second well. The third well could be due to parallel conduction in the doping regions deeper in the wafer, as one can see in Fig. 3.1. This third well exhibited capricious

behaviour by appearing and reappearing in a manner not yet understood. Sweep rates, exposure to various light sources such as a simple flashlight, the 1000 K globar, and covering the device with aluminum foil all demonstrated cause-effect results, but in no way were these procedures repeatable or consistent.

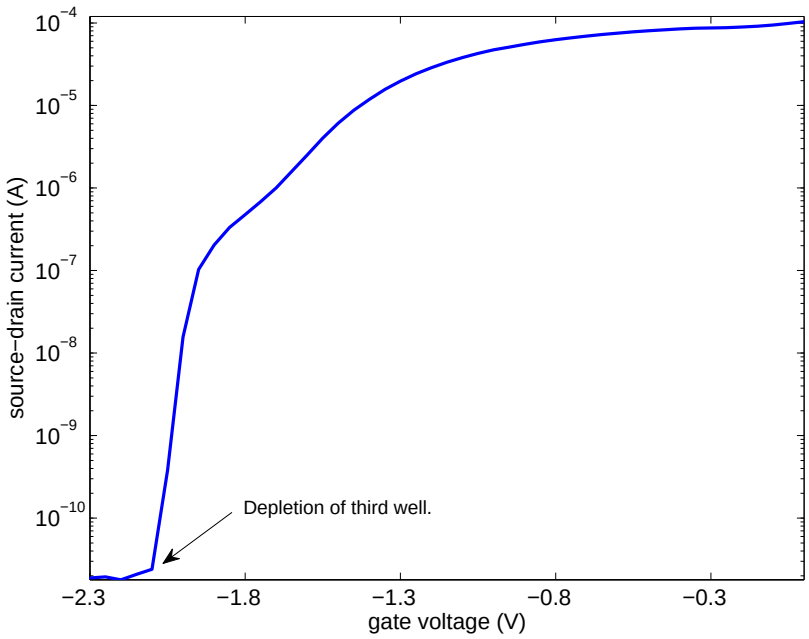

Fig. 5.5 I-V curve, $V_{DS} = 50$ mV, ambient light, 10 K. The third well is evident.

From the I-V curve in Fig. 5.4, one can infer the mobilities and carrier densities of the devices. Using a parallel-plate capacitive model for the charge densities in the two wells, we can state the charge density Q, as

$$Q = C\Delta V_{GS}, \tag{5.1}$$

where C:

$$C = \frac{\epsilon A}{d}. \tag{5.2}$$

ϵ is the permittivity of the well material (GaAs), $\approx 13 \cdot \epsilon_0$, and d is the distance from the Schottky gate at the semiconductor surface to either the top or bottom quantum well. ΔV_{GS} is the gate voltage required to deplete the top or bottom well under the Shottky gate.

Using the carrier density:

$$n = \frac{V_{GS} \cdot \epsilon}{de}, \tag{5.3}$$

we can find the mobility:

$$\mu = \frac{\sigma}{ne} = \frac{I_{DS}}{V_{DS} \cdot n \cdot e} \left(\frac{L}{W} \right), \tag{5.4}$$

Here, I_{DS} is the source-drain current, V_{DS} is the source-drain bias, and $\frac{L}{W}$ is the ratio of the length to the width of the conducting mesa between the two ohmic contacts.

Table 5.1 lists the top and bottom electron densities ($n_{s,top}$ and $n_{s,bot}$), and the electron mobilities in the top and bottom wells (μ_{top} and μ_{bot}). The source-drain resistance, $R = \frac{V_{DS}}{I_{DS}}$, is stated at zero gate voltage. All values are calculated for the device at 10 K with a source-drain bias of 50 mV, exposed to the globar light through a KRS-5 window.

The source-drain current for the same biasing conditions is higher or lower for different lighting conditions, as expected due to photoionization. From Fig.5.6, we see that the highest I_{DS} is present while the device is exposed to the globar only through the KRS5 window, since the sample is still seeing visible light because the KRS5 window transmits $0.6 - 40$ μm. Using the $12 - 20$ μm filter, one sees the current

Table 5.1 Experimental carrier density, mobility, and resistance at 10 K, $V_{DS} = 50$ mV. R is stated for $V_{GS} = 0\ V$.

Temp. (K)	$n_{s,top}$ (/cm^2)	$n_{s,bot}$ (/cm^2)	μ_{top} (cm^2/V·s)	μ_{bot} (cm^2/V·s)	R (Ω)
10	1.38×10^{11}	3.15×10^{11}	5.86×10^5	2.29×10^5	676

decrease slightly, as the device is now only responding to the THz radiation. When a mirror is placed over the KRS5 window, the device sees the minimal blackbody radiation from a 300 K source with very low emissivity, and the current is still lower.

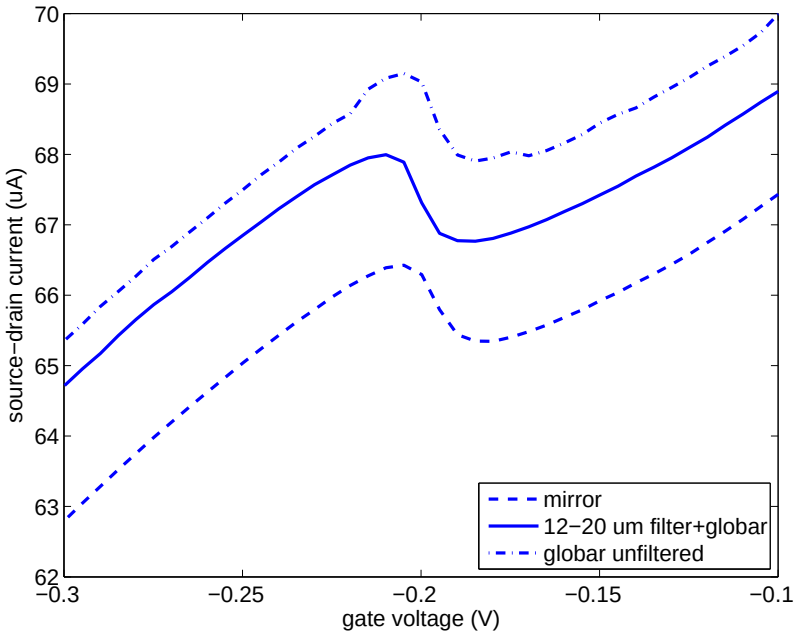

Fig. 5.6 I-V curve, $V_{DS} = 50$ mV, 10 K, KRS5 window. The device is subjected to different illumination conditions.

5.3 Lock-in amplifier measurements

An SR830 DSP Lock-in amplifier was employed to measure the response of the device to the 1000 K globar radiation through an optical chopper, whose chopping frequency was used as the reference frequency for the lock-in. A Labview program was written to automate data collection and the photoconductive response was measured for various biasing and lighting conditions.

In Fig. 5.7 we see the peak in photoconductive current occuring at ≈ 0.2 V, exactly where the slight rise in current occurs in the I-V curve (Fig. 5.4). Response was measured through a $12-20$ μm interference filter (Spectrogon 713MO3148), a $7-14$ μm interference filter (Spectrogon 713MO3147), and a Si wafer filter. The response is highest for the $12-20$ μm filtered light, and lowest for the Si filter, with the $7-14$ μm filter curve lying only slightly below the $12-20$ μm filter curve and so not illustrated for clarity purposes. The $12-20$ μm filter allows the highest photoresponse because only the light to which the device is most sensitive is transmitted, without any additional incident power that leads to device saturation. In future work we will use a monochromator to determine the spectral response of the device.

Through the course of the investigations it has been concluded that every cool-down, although performed in the same manner, gives slightly different response. This is most likely due to different dopant ionization ratios. Thus, the peak photoresponse for the $12-20$ μm filtered light varies from $10-25$ nA. However, the relative magnitude of response between all the filters is consistent for every cool-down.

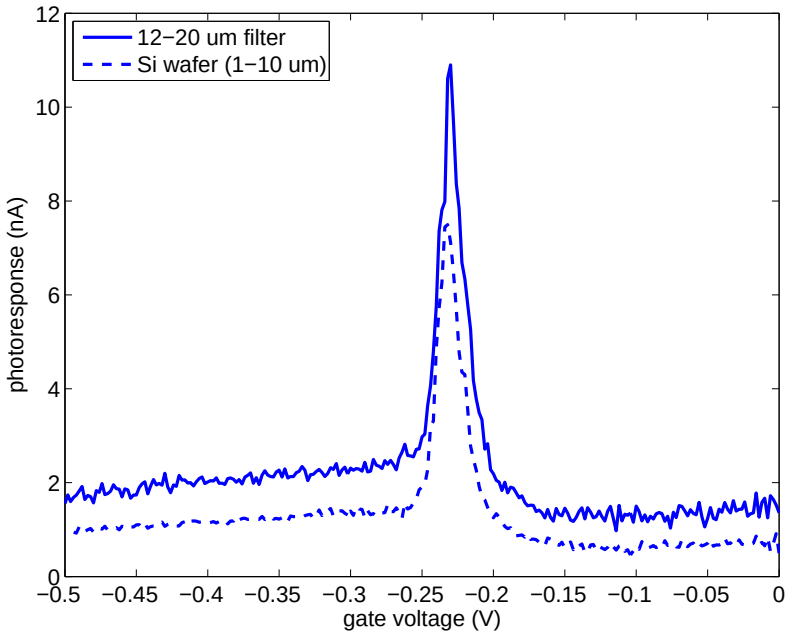

Fig. 5.7 Response to filtered globar light at a chopping frequency of 560 Hz, $V_{DS} = 50$ mV, 10 K.

We estimated the radiant power from the globar incident on the photoactive region of the sample to be $0.2 - 0.4$ nW. This calculation used Planck's Law to find the power emitted by the globar and accounted for the light losses along the optical path, such as the limiting aperture of the focusing mirror. The power was calculated for the $12 - 20$ μm spectral range, corresponding to the transmission window of the filter that yielded the highest photocurrent. A far-infrared power meter is necessary to more precisely state the incident globar power; for now we simply state the upper and lower bounds. Taking into account reflection losses from the KRS5 and optical interference filters, we estimate the responsivity of the device, calculated from Eqn. 2.2, to be $\mathcal{R} = 80 - 160$ A/W at 10 K. This result falls within the upper range of responsivities demonstrated by typical QWIPs (refer to Table 2.1).

While An *et al.* demonstrated a responsivity of 10^3 A/W at 4.2 K, a major structural difference between their device and our device is the width of the gate region on top of the mesa (see Fig. 4.1). Namely, An *et al.* fabricated gates with 250 nm wide regions, while ours are 50 μm. In earlier work [49], An *et al.* demonstrated devices with larger gate widths, and achieved a responsivity of only 2 A/W. A wider gate region overlying the mesa forms a wider lateral potential barrier encountered by laterally tunneling electrons, which leads to on-off switching of electron current rather than the fine control necessary to tune lateral tunneling rates and hence the electron density in the top well. Narrower confining gates need to be fabricated using electron-beam lithography techniques, which will be executed in future work. However, despite this structural drawback, we already demonstrate a responsivity almost 100 times higher than that of An *et al.*'s work with gate regions of similar width.

In Fig. 5.8, we see that the device response is approximately the same over chopping frequencies from 20 Hz to 1 kHz, the frequency limits of our optical chopper. The response was also measured at 70, 140, 280, and 560 Hz, with similar results. The device exhibits excellent bandwidth compared with Komiyama's group in Japan: the photoresponse reported in [12] peaked at a chopping frequency of 7 Hz, fell to approximately half its peak value at 23 Hz, and effectively disappeared at only 97 Hz.

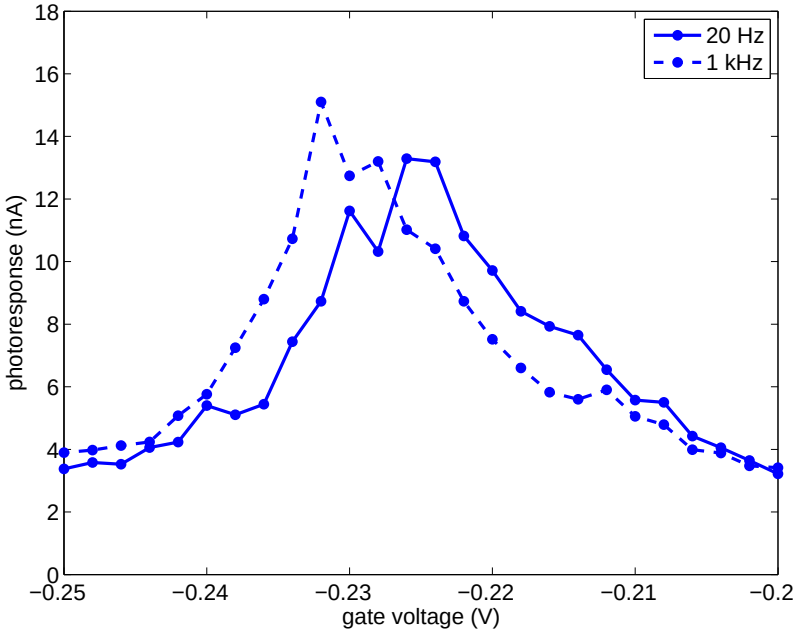

Fig. 5.8 Chopping requency response, $V_{DS} = 50$ mV, 10 K, KRS5+12−20 μm filter

Varying the source-drain bias changes the photoresponse, as seen in Fig. 5.9. Here, we see the response increase from a source-drain bias of 10 mV to 50 mV, as the electrons are experiencing a higher electric field, and hence higher photoconductive gain is achieved by the reduction in electron transit time through the active region. At source-drain biases beyond 50 mV, the response decreases due to increased phonon scattering of the electrons as the lattice is heated by the source-drain current itself. At 100 mV, scattering dominates and the photoresponse is barely noticeable.

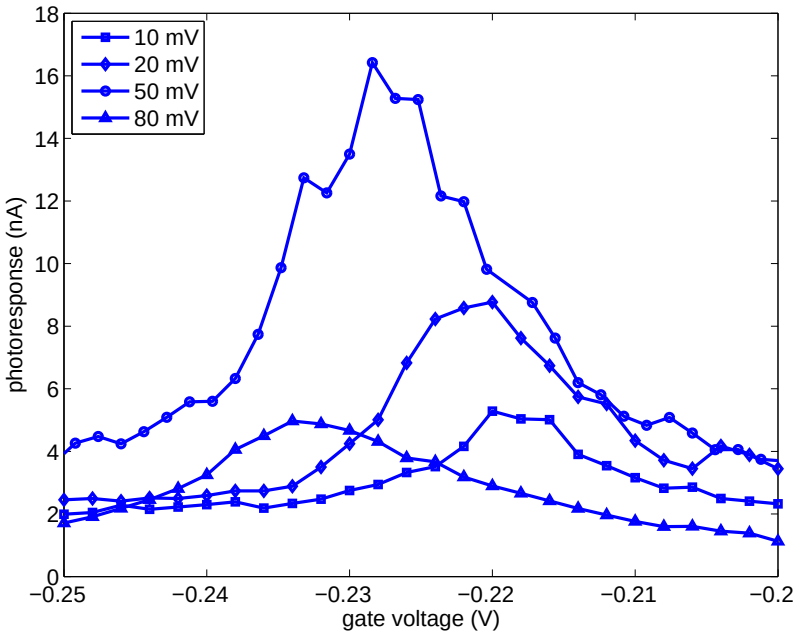

Fig. 5.9 Source-drain bias response, KRS5+12 − 20 μm filter, 560 Hz.

The temperature dependence of the photoresponse can be seen in Fig. 5.10. The response gradually decreases as temperature increases, due to increased phonon scattering and higher thermal excitation of the inter-subband transitions that are used for photodetection, and the photoresponse is barely discernible at 40 K.

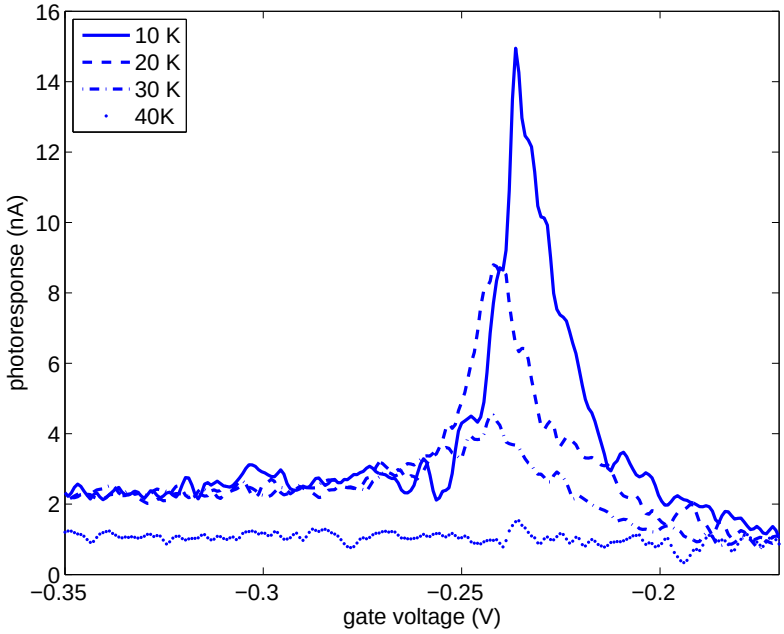

Fig. 5.10 Temperature response, KRS5+12 − 20 μm filter, 560 Hz, $V_{DS} = 50$ mV.

5.4 Noise spectral density and detectivity

In order to quantify the minimum detectable light signal, the source-drain current of the device was sampled at a frequency of 10 kHz for $V_{DS} = 50$ mV and $V_{GS} = -0.223$ V, conditions producing the peak photoresponse. The measurement was conducted with the device exposed only to the darkened room through the KRS5 window. A windowed FFT of the this noise data was performed in Matlab in order to extract the noise spectral density.

In Fig. 5.11 we see the noise spectral density, with lower frequency peaks occuring in multiples of power line cycles, as expected. From Eqn. 2.14, the NEP $= 4.7 \times 10^{-11}$ W/$\sqrt{\text{Hz}}$, and from Eqn. 2.15, we get D* $= 1.7 \times 10^{8}$ cm$\sqrt{\text{Hz}}$/W. These values

lie slightly below the range expected for typical QWIPs (refer to Table 2.1), but we will further investigate the noise mechanism in future work to improve the NEP.

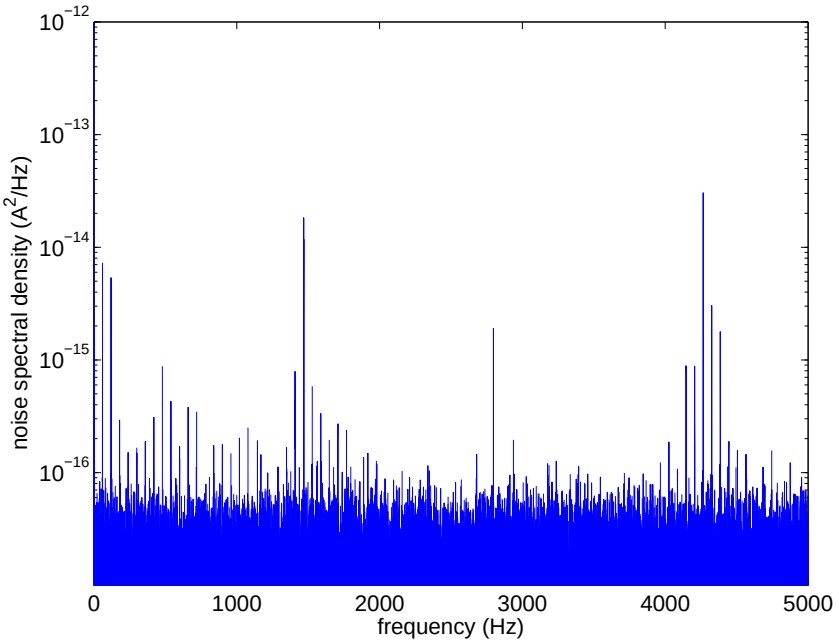

Fig. 5.11 Noise spectral density upon exposure to a dark room, 10 K, $V_{DS} = 50$ mV.

Chapter 6

Conclusions and future work

6.1 Summary

Detectors and sources in the THz wavelength range are comparatively new and undergoing much research to improve responsivity, detectivity and integration into imaging arrays. With applications including illegal substance detection, security, material characterization, and biomedicine, efficient THz detectors promise to give rise to important new industries.

We have fabricated and tested a GaAs/AlGaAs double quantum well heterostructure based on a floating gate architecture first developed by Komiyama [12] for ultrasensitive THz detection. The double-quantum well structure was designed and simulated using a 1-D Schrödinger-Poisson solver program and the wafer was commercially grown by molecular beam epitaxy. The photoconductor operates according to a perpendicular transport design, which provides greater photoconductive gain than the parallel transport typically employed by QWIPs. The detectors were fabricated using state-of-the-art fabrication facilities at Université de Montréal and McGill, and

tested under various temperatures and illumination conditions. We investigated fundamental properties of the device such as responsivity, sensitivity, and stability. Our device demonstrates the highest electrical bandwidth of a floating gate photoconductor (20 Hz $-$ 1 kHz, and possibly higher), and a responsivity better than conventional QWIPs ($\mathcal{R} = 80-160$ A/W). The photoconductive response is easily discernable up to 30 K. The device shows a NEP $= 4.7\times10^{-11}$ W/$\sqrt{\text{Hz}}$, and D* $= 1.7\times10^{8}$ cm$\sqrt{\text{Hz}}$/W.

6.2 Future work

This first detector illuminates the path for further exploration and improvement. Future work will consist of:

1. Record time resolved measurements to infer the upper frequency limit of the device using pulsed THz spectroscopy.

2. Analyze wavelength-dependent spectral response using a Cornerstone 74004 monochromator and compare the results with the calculated design wavelength of 12.4 μm.

3. Determine the effect of removing room temperature background blackbody emission by implementing a cold shutter inside the cryostat.

4. Describe the intrinsic noise mechanisms of the device. At present it is not known whether the noise is due to parallel conduction, poor material quality of the wafer, or other reasons. Once the noise properties of the device are better understood, we can surely increase the D* of the device.

5. Fabricate devices with narrow confining gates using electron-beam lithography, in order to exercise the fine control necessary to tune lateral tunneling rates and hence the electron density in the top well. With narrower confining gates, An *et al.* increased their responsivity by three orders of magnitude over devices with wider gates [49].

6. Address saturation issues: once a finite charge fills the bottom well, the conduction energy bands are altered and the device is effectively saturated. An *et al.* witnessed a responsivity ten times better using a reset gate to reverse device saturation [46]. We will create a new device design implementing a reset concept based on a pulsed-gate mode to increase the responsivity of the device.

7. Investigate methods to further increase operating temperature of the device. At present it is not understood what limits the operating temperature of the device, though QWIPs have been demonstrated to function up to 65 K [34]. One encouraging property of QDOTs is the low dark current due to 3-D confinement, which in turn allows higher operating temperatures, as demonstrated by the room temperature operation of the tunneling QDIP (T-QDIP) in [50]. The authors also report a THz T-QDIP operating at 150 K with a responsivity of ≈ 4 mA/W. A possible idea for a new higher-temperature design could be based on integrating a DWELL structure, utilizing the aforementioned advantages described in Section 2.2.8, with tunneling barriers to block the dark current carriers, as in [50].

8. Increase the quantum efficiency of the device through various radiation-coupling methods. Ideally, we seek to find a wavelength and size-independent coupling

scheme, such as merging the QWIP with a QDIP (quantum dot infrared photodetector). The advantage of such an arrangement is that the quantum dot will ensure that incident light normal to the wafer along the growth direction will cause intraband absorption [42].

Once the current device is fully characterized, we will pursue improvement of the parameters demonstrating the highest promise of successful optimization; for example, high-temperature operation, highest responsivity, etc. Device-to-device variation will be analyzed and minimized in order to construct a focal plane array of these optimized devices to serve as one of the first practical THz cameras in existence.

References

[1] B. Ferguson and X.-C. Zhang, "Materials for terahertz science and technology," *Nature Materials*, vol. 1, pp. 26–33, 2002.

[2] R. M. Woodward *et al.*, "Terahertz pulse imaging in reflection geometry of human skin cancer and skin tissue," *Phys. Med. Biol.*, vol. 47, no. 21, pp. 3853–3863, 2002.

[3] M. van Exter and D. Grischkowsky, "Characterization of an optoelectronic terahertz beam system," *IEEE Trans. Microwave Theory Tech.*, vol. 38, pp. 1684–1691, 1990.

[4] D. Grischkowsky, S. Keiding, M. van Exter, and C. Fattinger, "Far-infrared time-domain spectroscopy with terahertz beams of dielectrics and semiconductors," *J. Opt. Safety Am.*, vol. B7, pp. 2006–2015, 1990.

[5] H. Zhong, N. Karpowicz, J. Xu, Y. Deng, W. Ussery, M. Shur, and X. Zhang, "Inspection of space shuttle insulation foam defects using a 0.2 THz Gunn diode oscillator," *Imaging and Imaging Applications, IEEE, Center for THz Research*, vol. P2.79, pp. 753–754, 2004.

[6] National Research Council, *Assessment of Millimeter-wave and Terahertz Technology for Detection and Identification of Concealed Explosives and Weapons*. The National Academies Press, 2007.

[7] J. Federici, B. Schulkin, F. Huang, D. Gary, R. Barat, F. Oiveira, and D. Zimdars, "THz imaging and sensing for security applications - explosives, weapons and drugs," *Semiconductor Science and Technology*, vol. 20, no. 7, pp. 266–280, 2005.

[8] K. Kawase, Y. Ogawa, Y. Watanabe, and H. Inoue, "Non-destructive terahertz imaging of illicit drugs using spectral fingerprints," *National Institute of Police Science, Optics Express*, vol. 11, no. 20, pp. 2549–2554, 2003.

[9] M. Brucherseifer *et al.*, "Label-free probing of the binding state of DNA by time-domain terahertz sensing.," *Appl. Phys. Lett.*, vol. 77, pp. 4049–4051, 2000.

[10] M. Nagel, B. Haring, M. Brucherseifer, and H. Kurz, "Integrated THz technology for label-free genetic diagnostics," *Appl. Phys. Lett.*, vol. 80, pp. 154–156, 2002.

[11] E. Dereniak and G. Boreman, *Infrared Detectors and Systems*. John Wiley and Sons, Inc., 1996.

[12] Z. An, T. Ueda, J. Chen, and S. Komiyama, "A sensitive double quantum well infrared phototransistor," *Journal of Applied Physics*, vol. 100, no. 044509, 2006.

[13] A. Rogalski, *Infrared Photon Detectors*. The International Society for Optical Engineering (SPIE), Bellingham, 1995.

[14] B. Saleh and M. Teich, *Fundamentals of Photonics*. John Wiley and Sons, Inc., 2 ed., 2007.

[15] R. Jones *Proc. IRIS 2*, no. 1, pp. 9–12, 1957.

[16] J. Lamarre, F. Désert, and T. Kirchner, "Background limited infrared and submillimeter instruments," *Space Science Reviews*, vol. 74, no. 1-2, pp. 27–36, 2004.

[17] P. Siegel, "Terahertz technology," *IEEE Transactions on Microwave Theory and Techniques*, vol. 50, no. 3, pp. 910–928, 2002.

[18] J. Hesler and T. Crowe, "Responsivity and noise measurements of zero-bias Schottky diode detectors," *18th Intl. Symp. Space Terahertz Techn., Pasadena, March*, 2007.

[19] W. Peatman, T. Crowe, and M. Shur, "A novel Schottky/2-DEG diode for millimeter- and submillimeter-wave multiplier applications," *IEEE Electron Device Letters*, vol. 13, no. 1, pp. 11–13, 1992.

[20] M. Golay, "A pneumatic infra-red detector," *Rev. Sci. Inst.*, vol. 18, p. 357, 1947.

[21] D. Andrews, R. Milton, and W. DeSorbo, "A fast superconducting bolometer," *J. Opt. Soc. Amer.*, vol. 36, no. 9, pp. 518–524, 1946.

[22] W. Boyle and K. Rogers, "Performance characteristics of a new low-temperature bolometer," *J. Opt. Soc. Amer.*, vol. 49, pp. 66–69, 1959.

[23] F. Low, "Low-temperature Germanium bolometer," *J. Opt. Soc. Amer.*, vol. 51, pp. 1300–1304, 1961.

[24] M. Kinch and B. Rollin *Brit. J. Appl. Phys.*, vol. 14, p. 672, 1963.

[25] H. Drew and A. Sievers, "A 3He-cooled bolometer for the far infrared," *Applied Optics*, vol. 8, no. 10, p. 2067, 1969.

[26] A. Woodcraft *et al.*, "First tests of prototype SCUBA-2 superconducting bolometer array," *Proceedings of the AIP Conference, 24th International Conference on Low Temperature Physics*, vol. 850, pp. 1611–1612, 2006.

[27] SciTec Instruments, "http://www.scitec.uk.com/infrared_detectors/faq.php," *Retrieved April 25, 2009*.

[28] M. Dyakonov and M. Shur, "Shallow water analogy for a ballistic field effect transistor: New mechanism of plasma wave generation by dc current," *Phys. Rev. Lett.*, vol. 71, pp. 2465–2468, 1993.

[29] J. Lu and M. Shur, "Terahertz detector utilizing two-dimensional electronic fluid," *IEEE Electron Device Letters*, vol. 19, no. 10, pp. 373–375, 1998.

[30] A. Fatimy *et al.*, "Terahertz detection by GaN/AlGaN transistors," *Electronics Letters*, vol. 42, no. 23, 2006.

[31] L. Esaki and L. Chang, "New transport phenomenon in a semiconductor superlattice," *Phys. Rev. Lett.*, vol. 33, no. 8, pp. 495–498, 1974.

[32] L. Esaki and R. Tsu, "Superlattice and negative differential conductivity in semiconductors," *IBM J. Res. Develop.*, pp. 61–65, 1970.

[33] B. Levine, K. Choi, C. Bethea, J. Walker, and R. Malik *Appl. Phys. Lett.*, vol. 50, p. 1092, 1987.

[34] B. Levine, "Quantum-well infrared photodetectors," *J. Appl. Phys.*, vol. 74, no. 15, 1993.

[35] T. Faska *et al.*, "Innovative long wavelength infrared detector workshop," *Pasadena, CA, April 7-9*, 1992.

[36] K. Kheng *et al.*, "Two-color GaAs/(AlGa)As quantum well infrared detector with voltage-tunable spectral sensitivity at 3-5 and 8-12 μm," *Appl. Phys. Lett.*, vol. 61, no. 6, pp. 666–668, 1992.

[37] A. Rogalski, J. Antoszewski, and L. Faraone, "Third-generation infrared photodetector arrays," *J. Appl. Phys.*, vol. 105, 2009.

[38] D. Dooley, "THz intensity measurement... choose a Golay cell or a $LiTaO_3$ pyroelectric detector?," *Application Note, 100-1011, Spectrum Detector Inc.*, 2008.

[39] MicroTech Instruments, Inc. THz Detectors, "http://www.mtinstruments.com/thzdetectors/index.htm," *Retrieved May 28, 2009*.

[40] P. Norton, "HgCdTe infrared detectors," *Opto-electronics Review*, vol. 10, no. 3, pp. 159–174, 2002.

[41] A. Rogalski, "Third generation infrared detectors," *Proceedings of the Symposium on Photonics Technologies for 7th Framework Program, Wrocław, 12-14 October*, 2006.

[42] H. Liu, J. Duboz, R. Dudek, Z. Wasilewski, A. Fafard, and P. Finnie, "Quantum dot infrared photodetectors," *Physica E: Low Dimensional Systems and Nanostructures, Proceedings of the International conference on superlattices, nanostructures, and nano-devices*, vol. 17, pp. 631–633, 2003.

[43] S. Komiyama *et al.*, "A single-photon detector in the far-infrared range," *Nature*, vol. 405, pp. 405–407, 2000.

[44] S. Krishna, "Quantum dots-in-a-well infrared photodetectors," *Infrared Physics and Technology*, vol. 47, no. 1-2, pp. 153–163, 2005.

[45] J. Andrews *et al.*, "Comparison of long-wave infrared quantum-dots-in-a-well and quantum-well focal plane arrays," *IEEE Transactions on electron devices*, vol. 56, no. 3, pp. 512–516, 2009.

[46] Z. An, T. Ueda, K. Hirakawa, and S. Komiyama, "Reset operation of quantum-well infrared phototransistors," *IEEE Transactions on electron devices*, vol. 54, no. 7, 2007.

[47] J. Davies, *The Physics of Low-Dimensional Semiconductors*. Cambridge University Press, 1998.

[48] R. Williams, *Modern GaAs Processing Methods*. Artech House Inc., 2 ed., 1990.

[49] Z. An, J. Chen, T. Ueda, and S. Komiyama, "Infrared phototransistor using capacitively coupled two-dimensional electron gas layers," *Applied Physics Letters*, vol. 86, no. 172106, 2005.

[50] G. Ariyawansa, A. Perera, X. Su, S. Chakrabarti, and P. Bhattacharya, "Multicolor tunneling quantum dot infrared photodetectors operating at room temperature," *IEEE Transactions on electron devices*, vol. 50, pp. 156–157, 2007.